electronics

MDPI

Review

Technological Advances in GNSS Wave Buoys: A Review

Aolong Zhu [1], Kefeng Mao [1,*], Dongzhe Wang [2], Xi Chen [1] and Ming Li [1]

[1] College of Advanced Interdisciplinary Studies, National University of Defense Technology, Nanjing 211101, China; z15634137358@163.com (A.Z.); chenxi17@nudt.edu.cn (X.C.); liming17c@nudt.edu.cn (M.L.)
[2] Troops 96412, Chinese People's Liberation Army, Kunming 650217, China; 15987123846@163.com
* Correspondence: maokefeng@nudt.edu.cn

Abstract

This review examines Global Navigation Satellite System (GNSS) wave buoys from measurement principles and wave-parameter retrieval to representative systems and applications. By tracking buoy motion through three-dimensional position or velocity measurements, GNSS-based approaches offer diverse alternatives to conventional inertial-sensor buoys and potential for low-cost deployment at scale. We distinguish displacement-based from velocity-based methods according to their primary observables. Reference-station-dependent displacement methods can achieve positioning accuracies of 2–10 cm within approximately 50 km of shore, whereas Doppler and carrier-phase methods have reported velocity measurement accuracies of approximately 2–20 cm/s and 2–10 mm/s, respectively. These velocity-based methods offer potential for open-ocean deployment, provided that velocity observations are integrated or converted in the spectral domain. Our synthesis indicates that accuracy of displacement retrieval within the target wave band provides a more meaningful basis for comparing methods than raw-observation accuracy alone. Measurement errors do not necessarily propagate proportionally into derived wave parameters, with significant wave height and mean wave period generally showing good agreement across approaches. However, platform-dependent motion response limits the frequency range over which sea-surface motion can be reliably resolved. GNSS wave buoys already support in situ monitoring, satellite-product validation and wave-forecast evaluation; advances in accuracy and lighter platforms could broaden their use.

Keywords: GNSS buoy; wave observation; wave-parameter retrieval

Academic Editor: Silvia Liberata Ullo

Received: 30 September 2026
Revised: 07 November 2026
Accepted: 13 November 2026
Published: 16 November 2026

Copyright: © 2026 by the authors. Licensee MDPI, Basel, Switzerland. This article is an open access article distributed under the terms and conditions of the Creative Commons Attribution (CC BY) license.

1. Introduction

Wave observations are essential for marine hazard mitigation, navigation safety and climate research. Current approaches are commonly divided into remote sensing and in situ measurements [1]. Remote sensing techniques, including satellite altimetry and synthetic aperture radar (SAR), provide broad spatial coverage of wave fields, but their products remain affected by nonlinear retrieval and directional ambiguity. These estimates therefore require validation against high-accuracy in situ measurements. Buoys are widely regarded as the most reliable in situ benchmark for wave measurement. However, conventional buoy systems often rely on accelerometers and other sensor combinations, making them costly and difficult to deploy and maintain [2,3]. Global Navigation Satellite System (GNSS) buoys have therefore attracted increasing interest, because they can

directly measure three-dimensional displacement or velocity at relatively low cost and with simpler deployment [4].

Early GNSS buoy studies were primarily developed for tsunami warning, tidal datum determination, and water-surface elevation monitoring. DeLoach (1995) first mounted a GPS receiver on a navigation buoy to determine tidal datums [5]. Kato et al. (2000, 2001) then developed and refined a tsunami observation system using real-time kinematic GPS (RTK-GPS) (Trimble Inc., Westminster, CO, USA) [6,7]. Nagai (2005) further demonstrated the high precision of GPS buoys for tsunami waveform observation [8]. In parallel, GNSS buoys have increasingly been explored for wave observation. Existing approaches can be broadly grouped by the measured quantity into displacement-based and velocity-based methods. Displacement-based methods derive wave parameters from GNSS-positioned three-dimensional buoy motions, whereas velocity-based methods estimate wave-induced motion directly or indirectly from Doppler frequency-shift observations.

Displacement-based GNSS wave measurements generally use two positioning strategies. The first relies on shore-based reference stations, including differential positioning (DGPS/DGNSS), real-time kinematic positioning (RTK) and post-processed kinematic positioning (PPK). The second operates without a local reference station and includes single point positioning (SPP) and precise point positioning (PPP). Early displacement-based GNSS wave measurements relied mainly on DGPS and PPK, which can provide centimeter-level accuracy. Their offshore use is nevertheless constrained by the effective range of shore-based reference stations, which is typically less than 50 km [9,10]. PPP has therefore expanded the potential of GNSS buoys for open-ocean wave observation by reducing this dependence on coastal infrastructure. Bender et al. (2010) demonstrated the reliability of PPP and PPK for retrieving wave parameters under nearshore conditions [11]. Kuo (2012) compared DGPS, PPP and tide-gauge records, showing that PPP can resolve centimeter-scale sea-surface variations [12]. Lin (2018) developed a GNSS buoy that integrated virtual base station (VBS) and RTK techniques for real-time tidal-level and wave-data acquisition in estuarine and nearshore waters [10]. Shan et al. (2018, 2019) combined RTK, PPP and PPK dynamic positioning for wave measurements [13,14]. Gendron (2019) further compared the accuracy of PPK, PPP and time-relative positioning (TRP) for wave measurements using a small GNSS buoy [15]. SPP offers a lower-complexity alternative because it uses the position time series from a single GNSS receiver. Harigae et al. (2005) achieved centimeter-level measurements of wave height and wave direction using a commercial GPS receiver [16]. Joodaki (2013) subsequently introduced high-pass filtering to improve SPP-based wave-parameter retrieval [17]. Herbers et al. investigated an SBAS-enhanced single-receiver absolute positioning approach and demonstrated the feasibility of low-cost GNSS wave buoys [2]. Waseda (2014) used SPP to observe an extreme wave event [18].

Velocity-based GNSS wave measurement can be traced to the Seatex Smart-800 buoy (Seatex AS, Trondheim, Norway) reported by Krogstad et al. (1999), which derived three-dimensional velocity time series from differential GPS Doppler observations and demonstrated reliable performance in sea trials [19]. Datawell subsequently developed the DWR-G buoy, which uses a single GPS receiver to estimate buoy velocity from Doppler frequency shifts. Side-by-side comparisons with a conventional accelerometer-based DWR buoy showed close agreement in the principal wave parameters measured by the two systems [9]. Hou et al. (2006) applied a velocity-integration approach based on carrier-phase differential observations to wave-direction measurements, although the method relied largely on post-processing [20]. Doong et al. (2011) incorporated GPS-derived velocities into spectral analysis, retrieving wave parameters by converting velocity spectra into displacement spectra and applying directional wave-spectrum theory [21]. Thomson (2012) used GNSS Doppler observations to resolve wave-induced relative horizontal velocities from drifting buoys. However, limited vertical-velocity accuracy and sensitivity to

platform attitude required additional constraints from pressure and attitude sensors or filtering-based preprocessing [22]. A compact wave buoy developed by the Scripps Institution of Oceanography derived buoy velocities from GPS Doppler observations and was evaluated during a relatively large-scale field campaign in 2016 [23]. Qi (2019) further improved wave-measurement accuracy by using a neural network to correct anomalous velocity observations and incorporating Gaussian low-pass filtering into wave-spectrum processing [24].

Recent advances in GNSS wave buoys have followed three main directions. First, a growing range of positioning and velocity-estimation strategies has been evaluated. Zhu (2020) found that absolute height errors in PPP solutions have only a limited influence on wave-band spectra under low sea states, providing further support for PPP-based wave measurements [25]. Liu (2022) introduced an onboard GNSS variometric velocity-estimation method for real-time wave measurement [4]. Yang et al. (2024) subsequently developed a method based on single-frequency L1 time-differenced carrier phase (TDCP) observations, achieving accuracy comparable to PPK [26]. Xue et al. (2024) introduced the kinematic extension of the Variometric Approach for Displacements Analysis Stand-Alone Engine (Kin-VADASE), supporting the development of GNSS wave buoys towards real-time, lightweight, low-cost and networked operation [27]. Second, wave-parameter retrieval has expanded beyond conventional frequency-spectrum analysis. Gu et al. (2023) used three-dimensional displacement and velocity measurements from GNSS buoys to estimate both frequency and directional spectra, broadening their application to directional-spectrum analysis [28]. Peláez-Zapata et al. (2024) applied wavelet-based analysis to GPS-buoy observations, providing an alternative approach for estimating the directional distribution of waves [29]. Wang et al. (2025) proposed complementary statistical and spectral approaches that account for buoy-positioning resolution when extracting wave parameters [30]. Third, engineering development has increasingly emphasized low cost, miniaturization and rapid deployment. The Spotter buoy developed by Raghukumar et al. (2019) helped bring low-cost GNSS wave buoys with real-time capabilities into commercial use [31]. Thomson et al. (2024) developed and tested the expendable microSWIFT GNSS wave buoy for deployment from research aircraft, providing a low-cost platform for wave observations in extreme environments [32]. Collins et al. (2024) further showed that most small moored GNSS buoys offer adequate performance for nearshore engineering and wave-observation applications [33].

This review traces the development of GNSS wave-buoy technology, covering its methodological approaches, representative systems and applications. It further examines the accuracy characteristics of different buoy technologies, the effects of platform differences on wave-measurement performance and the suitability of buoys as external validation references, with the aim of informing future research and applications. This review focuses on technological developments in GNSS-based wave buoys over the past decade while also tracing the earlier studies that established the field. The literature search targeted GNSS-based wave buoys and covered three main themes: GNSS positioning and velocity-measurement techniques, wave-spectrum retrieval and wave-parameter estimation. Studies were selected according to their relevance to GNSS-based wave measurement and their representativeness in terms of technical methodology and experimental validation. Methodological studies were included to represent different GNSS observables and processing pathways. Experimental-validation studies were prioritized when they reported clearly defined reference measurements, sea-state conditions, processing frequency bands and quantitative evaluation metrics. Studies of representative systems and applications were selected to capture differences in technology approaches, buoy platforms and application contexts. Reported measurement performance was synthesized in the context of the corresponding experimental conditions and evaluation methods,

thereby clarifying the scope of validity of the reported results and the limitations of comparisons across studies.

The remainder of this paper is organized as follows: Section 2 describes the methods and technical approaches used to obtain GNSS buoy observations. Section 3 reviews wave-parameter retrieval methods and analyses error propagation across different buoy technologies. Section 4 introduces representative GNSS wave-buoy systems and their applications. Section 5 presents the discussion, and Section 6 concludes the review. Figure 1 summarizes the overall technical workflow for GNSS wave-buoy observations.

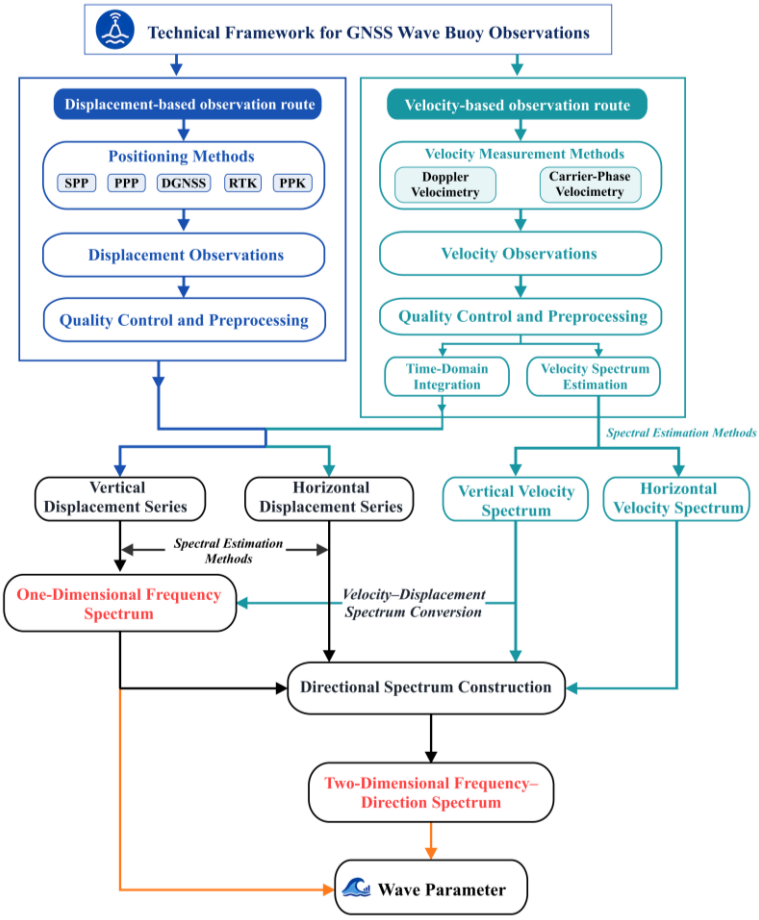


Figure 1. Technical workflow of GNSS wave buoys.

2. Acquisition Methods and Technical Approaches for GNSS Buoy Observables

GNSS buoy-based wave observation follows a continuous processing chain, from the acquisition of buoy-motion observables to the retrieval of wave parameters. This section reviews the methods and technical approaches used to acquire these observables and examines their applicability, providing the foundation for the wave-parameter retrieval methods discussed in the following section.

2.1. Technical Approaches for Displacement-Based GNSS Wave Buoys

2.1.1. Typical Positioning Strategies

GNSS positioning strategies provide the coordinate solutions required to construct a three-dimensional position time series of the buoy antenna. Here, these strategies are grouped into two categories: reference-station-dependent differential or relative positioning methods (DGPS, RTK and PPK) and single-receiver positioning methods that do not

require a shore-based reference station (SPP and PPP). The former generally yield higher-precision position estimates. Their reliance on shore-based infrastructure, together with the more involved data processing required by some implementations, can nevertheless constrain the open-ocean deployment of GNSS wave buoys. By contrast, single-receiver methods offer a simpler system architecture and greater deployment flexibility, making them attractive for low-cost and open-ocean observations. However, their positioning precision and capacity for error mitigation may affect the resulting wave-parameter estimates. Table 1 summarizes the technical characteristics of representative GNSS positioning strategies and their suitability for displacement-based wave measurements.

Table 1. Comparison of representative GNSS positioning strategies.

Positioning Strategy	Category	Technical Characteristics	Advantages	Limitations
SPP	Single-receiver positioning	Positioning from broadcast ephemerides and pseudoranges	Simple setup; flexible deployment	Limited accuracy; weak vertical stability
SBAS	Augmented single-receiver positioning	Satellite-correction-enhanced point positioning	No shore station; flexible regional deployment	Limited coverage and correction capability
PPP	Precise single-receiver positioning	Positioning with precise orbit and clock products	No shore station; suitable for open-ocean use	Convergence delay; dependence on precise products
DGNSS	Differential positioning	Reference-station pseudorange corrections	Higher accuracy than SPP	Shore-station dependence; limited open-ocean use
RTK	Real-time kinematic relative positioning	Real-time carrier-phase differential positioning	High accuracy; real-time output	Requires station and link; baseline-limited
PPK	Post-processed kinematic relative positioning	Post-processed carrier-phase differential positioning	High accuracy; no real-time link required	No real-time output; requires reference data

SPP uses a single GNSS receiver to determine an absolute position from pseudorange observations and broadcast ephemerides. Although simple and flexible to deploy, SPP is susceptible to measurement noise, satellite orbit and clock errors, atmospheric delays and multipath. Marine trials under open-sky conditions have reported absolute positioning accuracies of approximately 3–10 m [34–36]. PPP combines pseudorange and carrier-phase observations with precise GNSS products and error corrections, enabling high-accuracy positioning without a local reference station. It is therefore suitable for offshore wave-parameter retrieval and can achieve a positioning accuracy of approximately 3–10 cm under optimized processing conditions [12,37,38]. However, its dependence on precise products and processing strategies, together with the required convergence time, constrains short-duration observations, real-time applications and operation under complex sea states.

DGNSS applies reference-station corrections to pseudorange and range-rate observations, mitigating spatially correlated errors and producing more stable buoy position time series than SPP. It was used in early GPS wave-buoy systems and for directional wave observations in nearshore waters [39]. Its accuracy nevertheless degrades with increasing baseline length, while non-common errors at the buoy, including multipath and receiver noise, remain largely uncorrected [40]. SBAS extends differential correction coverage over much larger regions and mitigates distance-dependent errors across broad spatial scales. Although independent of local shore-based reference stations, it still relies on a wide-area network of ground monitoring stations and central processing facilities to generate corrections.

RTK combines carrier-phase differencing with integer ambiguity resolution to deliver centimeter-level kinematic positions in real time. It is well suited to trials in nearshore and harbor environments and has been widely applied to tidal-level, water-level and tsunami monitoring [6,41–43]. However, RTK depends on short baselines, stable

communication links and reliable ambiguity resolution. Longer baselines or communication interruptions can substantially reduce positioning continuity and reliability. Like RTK, PPK uses carrier-phase observations for relative kinematic positioning, but the two differ primarily in when solutions are generated. RTK applies corrections and outputs coordinates in real time, whereas PPK processes synchronized reference-station observations after data collection [44–46]. Its independence from real-time communication makes PPK suitable for high-accuracy retrospective analysis, intercomparison experiments and algorithm validation in GNSS buoy wave measurements [11,25]. Nevertheless, its accuracy remains sensitive to baseline length and post-processing strategy, and synchronized reference-station observations are still required. More generally, reference-station-based methods are constrained by baseline length. Vertical positioning accuracy can reach approximately 2–5 cm over short baselines, whereas errors typically increase to 5–10 cm when baselines extend to tens of kilometers [12,26,27,41,42].

GNSS absolute-positioning accuracy should not be taken as a direct measure of wave-measurement accuracy. GNSS-based wave measurement relies primarily on the time-varying positional changes induced by wave motion in the positioning sequence, rather than on the absolute position itself. Some positioning errors appear mainly as static biases or low-frequency drift and can therefore be attenuated through appropriate signal processing before wave retrieval. Consequently, substantial differences in the absolute-positioning accuracy of different GNSS methods do not necessarily lead to comparable differences in the retrieved wave parameters, which may still show good agreement.

2.1.2. Workflow for Processing Displacement Observations

In displacement-based approaches, GNSS processing yields a position time series for the buoy antenna in a geodetic coordinate system. This raw series generally cannot be directly interpreted as wave-induced displacement. Converting antenna positions to sea-surface elevations requires corrections for antenna mounting height and buoy attitude. The series also contains low-frequency variations and observational errors unrelated to wave motion. Raw displacement observations must first undergo quality control. Typical checks include solution status, valid-data proportion, sampling rate, missing samples, communication outages, abrupt jumps and gross outliers. These checks ensure sufficient continuity in the GNSS position or velocity time series. Horizontal observations subsequently require coordinate transformation because latitude and longitude do not directly represent buoy trajectories in a fixed local frame. They are therefore converted into local horizontal components for determining wave-propagation direction. Joodaki et al., for example, used the initial buoy position as the local origin and transformed GPS-derived latitude, longitude and height into a local east–north–height frame, as illustrated by Schematic A in Figure 2 [17]. Vertical observations require geometric correction because GNSS-derived heights refer to the antenna phase center. The offset between the antenna phase center and the waterline must therefore be measured and removed. Roll, pitch and antenna eccentricity introduce additional vertical motion that does not represent true sea-surface heave, as illustrated by Schematic B in Figure 2. These errors can be reduced through central antenna placement, lower mounting heights, attitude sensors or dynamic antenna-height calibration.

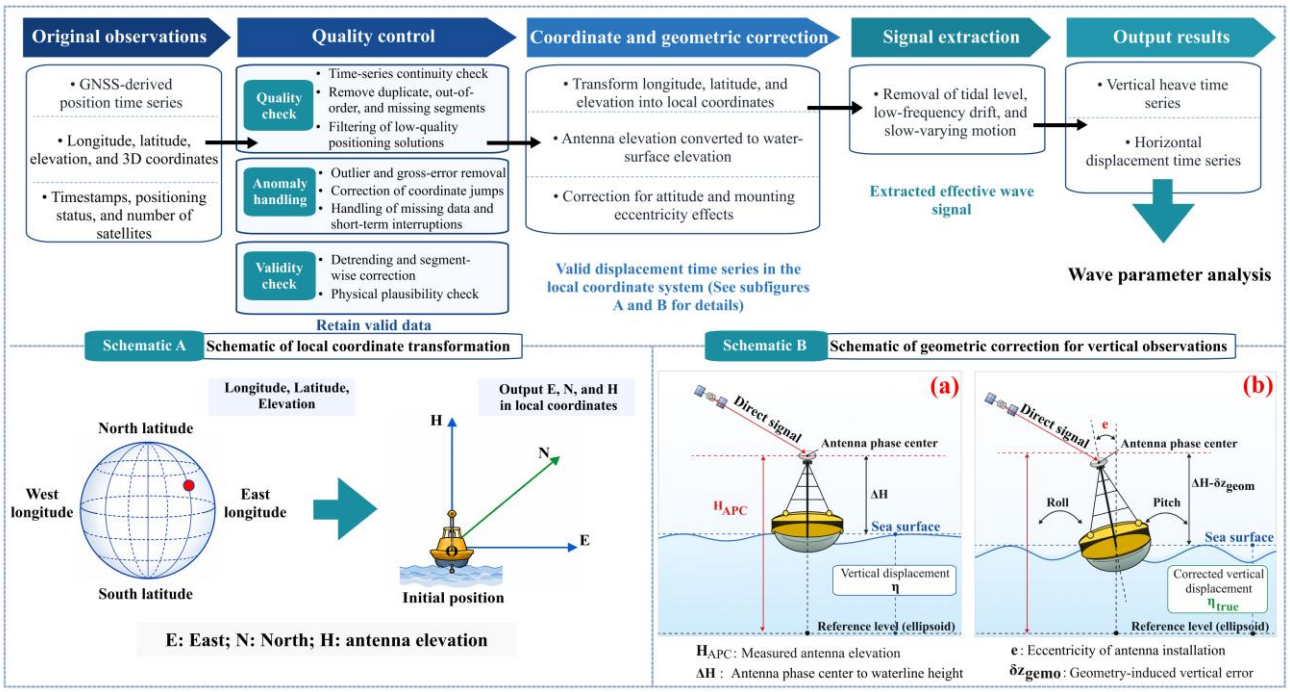


Figure 2. Technical workflow of the displacement-based approach. Schematic A illustrates the transformation to a local coordinate frame, whereas Schematic B shows the geometric correction applied to vertical displacement observations from a GNSS wave buoy. Schematic B (**a**) depicts antenna-height correction under ideal conditions, and Schematic B (**b**) identifies attitude- and installation-related geometric errors under non-ideal conditions.

Signal-separation techniques are commonly applied to displacement data to further suppress residual errors. High-pass filtering is widely used because GNSS positioning errors and wave-induced motion occupy partly distinct frequency ranges. GPS point-positioning errors are concentrated mainly below 0.01 Hz, whereas wind-wave-induced buoy motion generally occurs at higher frequencies. High-pass filtering can therefore attenuate tidal variability, low-frequency drift, slowly varying mooring motion and low-frequency positioning errors, isolating wave-induced displacement within the wave-frequency band [47]. Reported cutoff frequencies vary slightly, although most studies use 0.03 Hz, as summarized in Table 2. Joodaki evaluated several values, identifying optimal cutoff frequencies of 0.031 Hz under laboratory conditions and 0.011 Hz in field trials [17]. Figure 2 summarizes the overall workflow for processing displacement observations.

Table 2. High-pass filter cutoff frequencies used in selected studies.

Reference	GNSS Buoy Measurement Approach	Cutoff Frequency (Hz)
[17]	SPP	0.01, 0.03
[18]	SPP	0.03
[25]	PPP, PPK	0.02
[4]	Velocity-based approach	0.03
[9]	Velocity-based approach	0.03

2.2. Velocity-Based GNSS Buoy Techniques

2.2.1. Typical Velocity Estimation Methods

GNSS velocity estimation methods can be broadly classified as Doppler-based or carrier-phase-based. Doppler-based methods are widely used in velocity-based GNSS buoy systems and infer receiver velocity from the frequency shift induced by relative motion

between the satellite and receiver. Reported velocity accuracies range from approximately 2 to 20 cm/s [4,19,26,48]. This frequency shift reflects the satellite-receiver range rate along the line of sight [49]. Because each satellite provides only one line-of-sight velocity constraint, observations from multiple satellites must be combined with satellite positions, velocities and clock corrections. The receiver's three-dimensional velocity and clock-drift term can then be estimated using least-squares or filtering methods.

Carrier-phase-based velocity estimation has emerged as a high-precision approach for velocity-based GNSS wave buoys, with reported accuracies of 2–10 mm/s [4,48,50,51]. These methods determine short-term displacement increments by differencing carrier-phase observations between consecutive epochs and derive velocity by dividing the displacement by the sampling interval [52]. Representative implementations, including TDCP, the variometric approach and Kin-VADASE, have been applied to real-time wave observations. In the absence of cycle slips, integer ambiguities remain constant between consecutive epochs and are therefore eliminated by temporal differencing, while slowly varying errors are partly suppressed. Combining the resulting observations from multiple satellites enables the short-term three-dimensional displacement, and hence the velocity, of the buoy to be estimated.

2.2.2. Velocity-Observation Data Processing Workflow

Velocity-based GNSS wave buoys typically record three-dimensional velocity time series of wave-induced buoy motion, comprising one vertical and two orthogonal horizontal components. These observations are transformed into intermediate quantities that describe sea-surface elevation or wave-energy distributions, providing the basis for subsequent wave-parameter retrieval. Two main processing approaches have been developed. The first reconstructs buoy displacement by integrating the velocity time series in the time domain. For vertical motion, this relationship is expressed as Equation (1):

$$\eta(t) = \int w(t)dt \quad (1)$$

Here, $w(t)$ is the vertical velocity of the buoy, and $\eta(t)$ is the sea-surface elevation, or vertical displacement, reconstructed through temporal integration. Integrating the two orthogonal horizontal velocity components similarly yields the three-dimensional buoy displacement. The second approach operates directly on the velocity observations in the frequency domain. Spectral analysis is first applied to the velocity time series, after which the velocity spectrum is converted into a displacement spectrum using the frequency-domain relationship between velocity and displacement. This displacement spectrum characterizes the distribution of wave energy across frequencies.

Both approaches require stable velocity measurements within the wave-frequency band. The raw observations must therefore undergo quality control before integration or spectral conversion, following procedures broadly similar to those used in the displacement-based workflow. For velocity integration, low-frequency biases, mean offsets and non-wave-induced motion must be suppressed to prevent their accumulation as spurious displacement drift. For spectral conversion, the wave-frequency band must be isolated and spurious spectral peaks controlled to avoid amplifying velocity noise. High-pass filtering and appropriate smoothing are therefore commonly applied to define the analysis band and stabilize the resulting data.

Filtering should distinguish among measurement noise, low-frequency drift and anomalies in the observation time series, as these error sources require different treatments. Discontinuities caused by signal interruptions or anomalous velocity spikes should first be addressed through quality control to prevent them from introducing spurious low-frequency energy into subsequent spectral estimates. Persistent low-frequency noise can then be attenuated through detrending, high-pass filtering or band-pass

filtering. The choice of filtering scheme depends not only on the cutoff frequency but also on the filter order, transition-band characteristics and the frequency range used for subsequent spectral integration. Because genuine long-period swell and low-frequency measurement noise may occupy overlapping or adjacent frequency bands, a single fixed set of filter parameters may not be appropriate for all sea states. The processing range should therefore be selected by considering both the characteristics of the velocity noise and the target wave-frequency band. Figure 3 summarizes the processing workflow based on velocity observations.

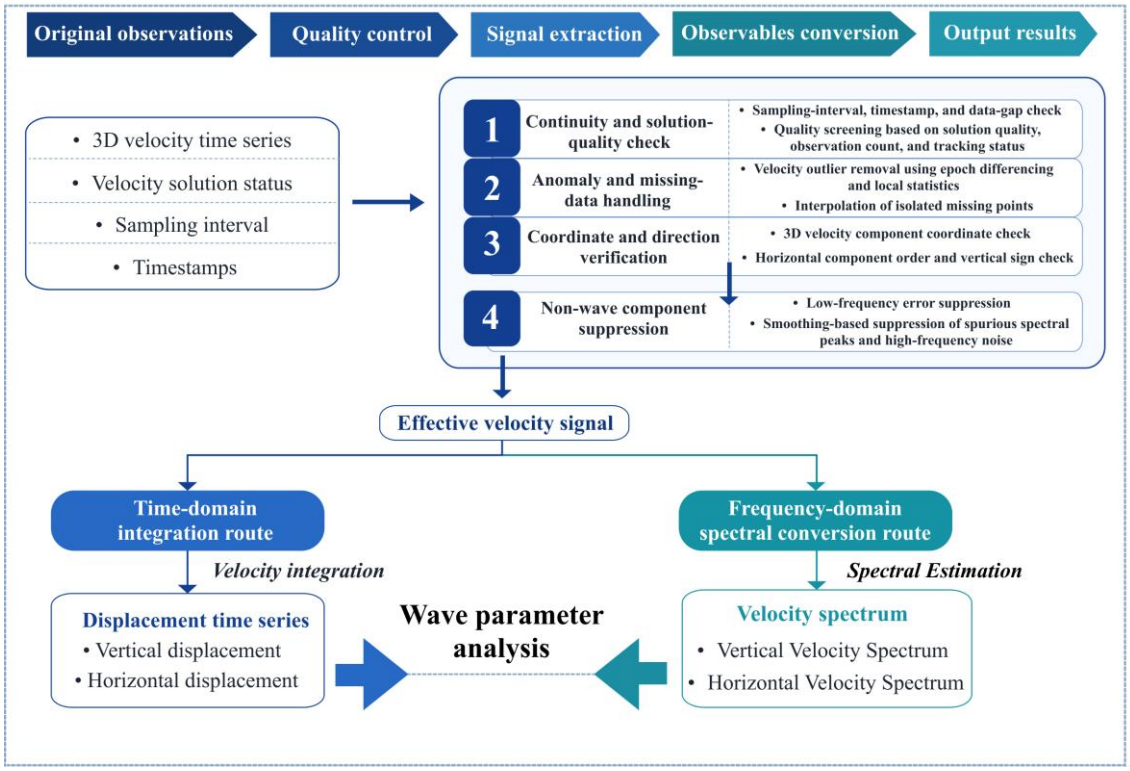


Figure 3. Technical workflow of the velocity-based approach.

2.3. Comparative Analysis

Displacement-based and velocity-based GNSS wave buoys both characterize wave-induced buoy motion for subsequent wave-parameter retrieval. However, they differ substantially in observable acquisition, data-processing pathways and implementation requirements. Table 3 compares the two approaches to clarify their technical characteristics and domains of applicability.

Table 3. Comparison of displacement-based and velocity-based GNSS wave-buoy approaches.

Comparison Criterion	Displacement-Based Approach	Velocity-Based Approach
Primary observable	Three-dimensional position time series	Three-dimensional velocity time series
Physical interpretation	Buoy heave and horizontal orbital displacement	Three-dimensional buoy velocity
Acquisition methods	SPP, PPP, DGNSS, RTK and PPK	Doppler and TDCP
Key processing steps	Positioning quality control; coordinate transformation; geometric correction	Velocity quality control; drift suppression; spectral processing
Main error sources	Positioning errors; multipath; antenna-height and attitude errors	Doppler noise; cycle slips; integration drift; spectral-conversion errors

Advantages	Direct physical interpretation	Favourable dynamic response; strong potential for real-time operation
Limitations	Complex error correction	Error accumulation or amplification during velocity conversion
Shore-based reference station	Required for DGNSS, RTK and PPK; not required for SPP or PPP	Generally not required

Table 3 highlights the complementary strengths and limitations of displacement-based and velocity-based GNSS wave buoys. Displacement-based approaches derive wave motion from position time series, providing a direct representation of buoy heave and horizontal displacement. Their range of positioning strategies also supports diverse deployment scenarios. In the open ocean, however, reference-station-independent methods involve trade-offs between accuracy and real-time performance. Vertical displacement estimates are also sensitive to antenna geometry and buoy attitude, complicating error correction. Velocity-based approaches, by contrast, offer favorable dynamic response and strong potential for real-time operation. Doppler- and carrier-phase-based methods generally do not require shore-based reference stations; when available, reference-station data or external corrections primarily improve velocity precision and stability. This independence provides greater deployment flexibility. Nevertheless, velocity must be related to sea-surface displacement through time-domain integration or frequency-domain spectral conversion, which can introduce error accumulation and noise amplification. These route-level differences alone do not determine the suitability of individual methods for specific applications. Table 4 therefore compares displacement- and velocity-acquisition methods against several key application factors.

Table 4. Suitability of GNSS wave-measurement methods across key operational criteria.

Key Criterion	Suitable Methods	Rationale
Open-ocean deployment	SPP, PPP, Doppler, TDCP	No local reference station or short baseline
High-accuracy displacement estimation	PPP, RTK, PPK	Centimeter to decimeter-level accuracy
Real-time capability	DGNSS, RTK, Doppler, TDCP	Real-time corrections or velocity estimation
Lower processing complexity	SPP, Doppler	Direct position or velocity outputs
Higher processing complexity	PPP, RTK, PPK, TDCP	Advanced corrections or carrier-phase processing
Low-cost, lightweight deployment	SPP, Doppler	Minimal infrastructure and hardware requirements

Table 4 shows that no GNSS observable-acquisition method is universally optimal; method selection instead depends on the observation objective, marine environment and engineering constraints. Open-ocean applications favor methods that are independent of local shore-based reference stations and short baselines. SPP and Doppler-based methods are particularly attractive for low-cost, lightweight deployment, whereas PPP provides higher positioning accuracy when suitable precise products and sufficient convergence time are available. For high-precision nearshore intercomparison, method validation or sea-surface elevation reconstruction, RTK and PPK are also advantageous. TDCP can achieve millimeter-per-second velocity precision, but its performance depends on continuous carrier-phase observations, reliable cycle-slip detection and adequate solution availability. PPK and conventional post-processed PPP are therefore unsuitable for real-time

wave monitoring. When both high precision and real-time operation are required, RTK, real-time PPP and TDCP-based velocity estimation are better suited.

3. Wave-Parameter Retrieval Methods for GNSS Buoys

Wave parameters quantify sea-surface variability and wave propagation. Their estimation generally follows two approaches: time-domain zero-crossing analysis of individual waves and spectral analysis of wave-energy distributions [53]. Zero-crossing analysis partitions a surface-elevation record at successive zero crossings to derive individual wave heights, periods and their statistics. However, a small set of bulk parameters cannot fully describe the sea state. In mixed seas containing both wind-sea and swell components, similar bulk wave heights and periods may mask markedly different energy partitioning and structures among wave systems [54,55]. By resolving wave energy across frequency, direction and wavenumber, spectral analysis therefore provides a more informative basis for wave-parameter retrieval from GNSS buoys [56].

3.1. Sea State Measurement Using the Wave Spectrum

3.1.1. Wave Spectrum Estimation Methods

Over short intervals and spatially limited domains, sea-surface elevation can often be approximated as a stationary random process [57]. Under linear stochastic wave theory, an irregular sea surface is represented as a superposition of harmonic components with different amplitudes, frequencies, phases and propagation directions [58]. Table 5 summarizes the principal methods for estimating the one-dimensional frequency spectrum $E(f)$ from observed time series. The periodogram, autocorrelation-function, Bartlett and Welch methods are classical Fourier-based estimators. Bartlett and Welch reduce estimation variance by segmenting the record and averaging the resulting periodograms, whereas autoregressive methods estimate the spectrum using a parametric model. Multitaper estimation balances spectral-leakage suppression against estimator variance, while wavelet spectral analysis and the Hilbert–Huang transform resolve the time-frequency structure of non-stationary wave processes. Incorporating propagation direction yields the two-dimensional frequency-direction spectrum $E(f,\theta)$, which describes the joint distribution of wave energy across frequency and direction. The one- and two-dimensional spectra are related by Equation (2):

$$E(f,\theta) = E(f)G(f,\theta) \tag{2}$$

Here, $G(f,\theta)$ denotes the directional spreading function. Equation (2) expresses the two-dimensional frequency-direction spectrum as the product of the one-dimensional frequency spectrum and the directional spreading function. When $G(f,\theta)$ is normalized over direction, integrating $E(f,\theta)$ with respect to θ recovers $E(f)$. The directional spreading function can be estimated using Equation (3):

$$G(f,\theta) = \frac{1}{\pi}\left[\frac{1}{2} + a_1\cos(\theta) + b_1\sin(\theta) + a_2\cos(2\theta) + b_2\sin(2\theta) + \cdots\right] \tag{3}$$

Equation (3) represents $G(f,\theta)$ as a Fourier series in θ, with a_1, b_1, a_2 and b_2 denoting the directional Fourier coefficients. These coefficients are typically estimated from the auto- and cross-spectra of synchronized motion components. Autospectra quantify the energy of each component across frequencies, whereas cross-spectra capture the amplitude correlations and phase differences between components, from which wave-propagation direction and directional spreading can be inferred. Conventional directional wave buoys analyse heave, pitch and roll records or the corresponding three-component acceleration signals [59]. GNSS buoys can instead use positioning-derived vertical and two orthogonal horizontal displacements, a combination of vertical displacement and two horizontal velocities or three-component velocity records. Multi-component spectral

analysis of these observations yields the directional Fourier coefficients and hence the directional spreading function [28].

It should be noted that the one-dimensional energy spectrum and the first four directional Fourier coefficients obtained from single-point, three-component motion observations, collectively referred to as the First Five, can be used to estimate statistical quantities such as the mean wave direction and directional spreading [60]. However, these coefficients contain only the first two orders of the Fourier representation of the directional distribution function and therefore cannot uniquely determine the full two-dimensional directional spectrum. When multiple wave systems overlap in similar frequency ranges, the limited directional information can also make it difficult to resolve closely spaced directional peaks. Previous studies have shown that under certain conditions, high-quality First Five data can distinguish two wave systems at the same frequency when their propagation directions differ by approximately 60° or more. The actual directional resolution, however, depends on the directional separation, relative energy and directional spreading of the wave systems, as well as on the spectral estimation method used [59]. Reconstructing the full directional distribution generally requires methods such as truncated Fourier-series, maximum entropy or maximum likelihood estimation. These methods nevertheless differ in both resolution and limitations. Direct truncation of the Fourier series may produce non-physical negative energy, whereas weighting schemes may excessively broaden the directional spectrum [61]. The maximum entropy method may generate overly narrow or spurious directional spectral peaks, while the smoothing inherent in maximum likelihood estimation may obscure closely spaced wave systems [62]. Accordingly, directional spectra inferred from GNSS buoy observations should be regarded as estimates jointly constrained by limited directional observations and the reconstruction method. In complex multimodal sea states with overlapping frequencies and propagation directions, the number, propagation directions and directional spreading of spectral peaks should therefore be interpreted with caution.

Table 5. Representative methods for estimating one-dimensional wave frequency spectra from observations.

Method	Principle	Advantages	Limitations	Reference
Periodogram method	Fourier transform of the observed record	Simple and intuitive; clear peak detection	Sensitive to spectral leakage and noise	[63]
Autocorrelation-function method	Fourier transform of the autocorrelation function	Suitable for stationary processes; clear physical basis	Sensitive to lag length, truncation and smoothing	[64]
Bartlett method	Average of periodograms from non-overlapping segments	Lower variance; smoother spectra	Reduced frequency resolution; limited data use	[65]
Welch method	Average of windowed periodograms from overlapping segments	Lower variance and leakage; widely applicable	Requires selection of window, overlap and segment length	[66]
Autoregressive spectral estimation	Parametric spectrum derived through linear prediction	High resolution for short records	Sensitive to model order; possible spurious peaks	[67]
Wavelet spectral analysis	Time-frequency energy derived through wavelet transforms	Suitable for non-stationary seas and wave-group evolution	Sensitive to mother wavelet, scale and boundary effects	[68]
Multitaper spectral estimation	Weighted average of spectra obtained using orthogonal tapers	Low leakage with stable estimates	Complex parameter selection	[69]
Hilbert-Huang transform	EMD followed by Hilbert analysis of instantaneous frequency and energy	Suitable for nonlinear and non-stationary waves	Mode mixing, end effects and non-unique decomposition	[70]

3.1.2. Wind-Sea and Swell Identification Methods

Once a wave spectrum has been retrieved from the observations, separating wind sea from swell helps resolve the structure of the sea state and improves the interpretation of complex wave conditions. For one-dimensional spectra, this separation relies primarily on selecting an appropriate separation frequency. Table 6 summarizes representative methods. Early approaches, including the PM and wave-steepness methods, used empirical criteria derived from fully developed wind-sea spectra, wave steepness or wind-speed constraints. Although simple and suitable for operational use, they are sensitive to wind input, assumptions about wind-sea development and spectral-peak structure. Later methods, such as JP and HP, combined spectral partitioning with wave-system identification rather than relying on a single separation frequency, improving their applicability to multimodal spectra and mature wind seas. More recently, deep-learning and probabilistic approaches have extended wind-sea and swell identification to one-dimensional spectra and other non-directional observations. These methods have modest data requirements, but uncertainty remains when wind sea and swell occupy similar frequency ranges while propagating in different directions.

Table 6. Wind-sea and swell separation methods for one-dimensional frequency spectra.

Method	Required Data	Core Principle	Advantages	Limitations	Reference
Pierson-Moskowitz peak-frequency method (PM)	$E(f)$; wind speed	Separation frequency from a fully developed wind-sea spectrum	Simple formulation	Requires wind speed and a fully developed wind sea	[71]
Wave-steepness method	$E(f)$	Separation frequency from the peak of a wave-steepness function	No wind or directional data required	Sensitive to spectral shape and swell fraction	[72]
Modified wave-steepness method	$E(f)$; wind speed	Wind-speed correction of the separation frequency	Fewer errors at low wind speeds	Requires empirical thresholds and wind data	[73]
Spectral partitioning and identification method (JP)	$E(f)$	Partition the spectrum, then identify wave-system attributes	Suitable for multimodal spectra	Limited for frequency-overlapping systems with different directions	[74]
Spectrum-integration method (HP)	$E(f)$	Separation frequency from weighted spectral integration	More stable than the wave-steepness method	Lacks directional resolution	[75]
Deep neural network method	$E(f)$; optional wind speed	Direct prediction of wind-sea and swell parameters	Captures nonlinear relationships	Depends on training data and regional representativeness	[76]
Probabilistic swell-identification method	Wave statistics or nondirectional data	Identification from joint probability relationships	Suitable without directional data	Depends on stable statistical relationships	[77]

Table 7 summarizes methods for separating wind sea and swell using two-dimensional wave spectra. Unlike one-dimensional frequency spectra, frequency-direction spectra resolve both wave frequency and propagation direction, enabling multiple wave systems to be distinguished in complex mixed seas. Most methods comprise two stages. The directional spectrum is first partitioned into wave systems associated with local spectral peaks. Each partition is then classified as wind sea or swell using wave age, the local wind vector, wind-input conditions or spectral-peak energy. Methodological development has progressed from directional partitioning and watershed segmentation to wave-system identification and tracking, model-based partitioning, overshoot detection and dynamic partitioning. Recent studies have further adapted these methods to finite-depth waters, strong winds, wave refraction and multi-source observations. By resolving directional differences, two-dimensional methods can distinguish wave systems that overlap in

frequency and therefore outperform one-dimensional methods in complex mixed seas. Their reliability nevertheless depends critically on directional-spectrum quality, concurrent wind data, water depth and algorithmic thresholds. For GNSS buoys, these benefits remain contingent on robust retrieval of the frequency-direction spectrum.

Table 7. Wind-sea and swell separation methods for two-dimensional frequency-direction spectra.

Method	Required Data	Core Principle	Advantages	Limitations	Reference
Spectral-partitioning algorithm (SPA)	$E(f,\theta)$	Local-peak-based wave-system partitioning	Foundational partitioning framework	Requires separate wind-sea/swell classification	[78]
Inverse catchment-area partitioning	$E(f,\theta)$	Assignment of spectral bins to local energy peaks	Suitable for multimodal spectra	Sensitive to noise peaks and thresholds	[79]
Optimal interpolation of partitions (OI-P)	$E(f,\theta)$ or partition parameters	Partition representation by energy, frequency and direction	Reduces spectral-assimilation dimensions	Depends on partition matching	[80]
Wave Identification and Tracking System (WITS)	$E(f,\theta)$; wind field	Partitioning, wave-age classification and swell tracking	Enables swell-source tracking	Depends on wind fields and thresholds	[81]
Wave Spectrum Energy Partitioning (WaveSEP)	$E(f,\theta)$; wind field	Wave-age-based wind-sea/swell classification	Suitable for operational model outputs	Strong dependence on empirical thresholds	[82]
Dynamic partitioning using sequential Monte Carlo	Time series of $E(f,\theta)$	Sequential tracking of wave-system evolution	Improves separation of adjacent systems	High computational complexity	[83]
Overshoot-phenomenon method	$E(f,\theta)$; partitioned spectra	Comparison with PM peak energy at the same frequency	No wind-field data required	Delayed response during growth and decay	[84]
HF-radar directional-spectrum partitioning	HF-radar-derived wavenumber–direction spectrum	Partitioning of radar-derived spectra	Reveals nearshore spatial variability	Sensitive to inversion accuracy and signal-to-noise ratio	[85]
Finite-depth WA/OP separation	$E(f,\theta)$; wind field; water depth	Finite-depth correction of WA/OP criteria	Suitable for shallow and finite-depth waters	WA threshold sensitivity; OP response lag	[86]
Duration-limited growth method	$E(f,\theta)$; wind field; depth; refraction data	Inclusion of growth duration and refraction	Reduces errors under strong winds and shallow-water conditions	Requires extensive environmental data	[87]

Several GNSS buoy studies have used 0.125–0.127 Hz to separate wind sea from swell. Comparisons with acceleration-based Datawell buoys show close agreement in partitioned significant wave height. Patra reported correlation coefficients of 0.97 for wind sea and 0.89 for swell, whereas Beckman obtained an RMSE of 0.05 m for both partitions and corresponding r^2 values of 0.98 and 0.92 [88,89]. Agreement was weaker for period and directional parameters. Beckman reported peak-period RMSEs of 1.14 s for wind sea and 4.79 s for swell, together with positive directional-spreading biases of 10.03° and 8.22°, respectively. The GNSS buoy also detected approximately 46% fewer multimodal directional-spectrum events than the Datawell buoy [89]. In a long-term comparison, the correlation in band-limited significant wave height between Spotter and Waverider fell to 0.49 within the 0.03–0.06 Hz band, with an RMSE of 0.15 m [90]. These results suggest that GNSS buoys can reliably recover integrated energy within wind-sea and swell partitions, whereas swell peak period, directional spreading and complex wave-system identification remain more sensitive to low-frequency response and directional resolution.

3.2. Conversion of GNSS Observables to Wave Spectra

For displacement-based GNSS buoys, vertical displacement is used to estimate the one-dimensional frequency spectrum, typically using Fourier-based spectral estimators.

Together with the vertical component, the two horizontal displacement components provide the directional information required to construct the two-dimensional frequency-direction spectrum. The orthogonal horizontal displacements are first transformed into a local east-north frame. Spectral analysis of the resulting vertical, eastward and northward displacement series then yields their auto-spectra and pairwise cross-spectra. Because the directional spreading function $G(f,\theta)$ can be expressed as a Fourier series in θ, these spectral relationships determine the directional Fourier coefficients and hence the distribution of wave energy over direction at each frequency.

As described in Section 2.2.2, velocity observations enter wave spectral analysis through either time-domain integration or direct frequency-domain conversion. In the first pathway, the vertical and horizontal velocity time series are integrated to obtain equivalent displacements, after which the standard displacement-based workflow applies. The vertical displacement yields $E(f)$, while the combined vertical and horizontal components determine $G(f,\theta)$ and hence $E(f,\theta)$. In the second pathway, spectra are estimated directly from the velocity records. For example, the vertical-velocity spectrum $S'_w(f)$ can be estimated from $w(t)$ using any of the methods listed in Table 5. The estimation framework is unchanged, but $S'_w(f)$ describes the frequency distribution of vertical-velocity variance rather than displacement variance. It can then be converted into an equivalent displacement spectrum using Equation (4).

$$S_\eta(f) = \frac{S'_w(f)}{(2\pi f)^2} \tag{4}$$

Here, $S'_w(f)$ denotes the vertical-velocity spectrum, $S_\eta(f)$ the vertical-displacement spectrum obtained from the velocity spectrum, corresponding to the one-dimensional wave frequency spectrum, and f the frequency. Because velocity is the first-order time derivative of displacement, the velocity and displacement spectra differ in the frequency domain by a frequency-dependent factor of $(2\pi f)^2$. The sea-surface elevation spectrum can therefore be recovered by applying the corresponding frequency-factor correction to the vertical-velocity spectrum. For the two-dimensional frequency-direction spectrum, the auto- and cross-spectral analysis described in Section 3.1.1 can be used to estimate the directional Fourier coefficients and subsequently construct the directional spreading function $G(f,\theta)$. Moreover, converting a velocity spectrum into a displacement spectrum does more than establish a frequency-domain relationship between the two observables. It also imposes frequency-dependent weighting on velocity-measurement errors. Equation (4) therefore describes both the transformation of the velocity signal into a displacement spectrum and the frequency-domain propagation of velocity-measurement errors. Because GNSS velocity observations inevitably contain measurement noise, the measured vertical velocity can be represented as the sum of the true velocity and an uncorrelated measurement-error term. The corresponding measured velocity power spectrum is then the sum of the true-velocity power spectrum and the power spectral density of the measurement error. Neglecting buoy dynamics and filter attenuation, the contribution of velocity-measurement errors to the reconstructed displacement spectrum is given by Equation (5).

$$\Delta S_\eta(f) = \frac{S_{e_v}(f)}{(2\pi f)^2} \tag{5}$$

Here, $\Delta S_\eta(f)$ denotes the additional spectral energy introduced into the reconstructed displacement spectrum by velocity-measurement errors, and $S_{e_v}(f)$ denotes the power spectral density of the vertical velocity-measurement error.

When the velocity-noise spectral density is comparable, the contribution of measurement error to the reconstructed displacement spectrum increases as frequency decreases, indicating a pronounced sensitivity to low-frequency noise. For example, reducing the frequency from 0.20 Hz to 0.05 Hz increases the corresponding displacement-spectrum

noise contribution by a factor of 16 for the same velocity-noise spectral density. The frequency-domain transformation applies the same frequency weighting to the true signal and measurement noise at a given frequency and therefore does not directly alter the signal-to-noise ratio at that frequency. It can nevertheless cause low-frequency measurement noise to appear as substantial spurious energy in the reconstructed displacement spectrum. In practical processing, high-pass filtering suppresses this spurious low-frequency energy but also affects the recovery of the true wave spectrum. A higher cutoff frequency may attenuate or remove the low-frequency energy associated with long-period waves, whereas a lower cutoff frequency retains more genuine wave energy at the cost of allowing more residual noise to enter the reconstructed spectrum. The recovery of low-frequency wave energy therefore depends not only on the velocity-to-displacement spectral conversion but also on the high-pass cutoff frequency and the filter's actual frequency response.

3.3. Wave-Parameter Retrieval from Wave Spectra

Significant wave height is a primary descriptor of sea state and a core output of GNSS wave-buoy analyses. Under linear stochastic wave theory, its spectral estimate is expressed as four times the standard deviation of sea-surface elevation. The zeroth spectral moment m_0, obtained by integrating the spectral density over the full frequency range, represents the variance of sea-surface elevation. Significant wave height can therefore be derived from the wave spectrum using Equation (6).

$$H_s = 4\sqrt{m_0} \tag{6}$$

Wave-period parameters are characteristic quantities derived from the frequency-domain wave spectrum. Common measures include the spectral-moment periods T_{m02}, T_{m01} and T_{m-10}, together with the peak wave period T_p, as defined in Equations (7)–(10). Defined from the zeroth and second spectral moments, T_{m02} closely approximates the time-domain mean zero-crossing period and is therefore widely used as a spectral measure of mean wave period. It is, however, sensitive to the high-frequency spectral tail. T_{m01} characterizes the mean frequency content of the full spectrum and is less sensitive to high-frequency energy. By placing greater weight on low-frequency components, T_{m-10} better captures the contribution of long-period waves and is particularly relevant to wave-energy flux and nearshore engineering. The peak period T_p, determined from the spectral peak frequency f_p, represents the energy-dominant wave system and can help identify the principal system in multimodal seas.

$$T_{m02} = \sqrt{\frac{m_0}{m_2}} \tag{7}$$

$$T_{m01} = \frac{m_0}{m_1} \tag{8}$$

$$T_{m-10} = \frac{m_{-1}}{m_0} \tag{9}$$

$$T_p = \frac{1}{f_p} \tag{10}$$

Here, m_n is the spectral moment of order n, as defined in Equation (11):

$$m_n = \iint f^n E(f,\theta) df d\theta \tag{11}$$

The principal wave-direction parameters are the peak and mean wave directions. The peak direction represents the dominant wave system and is determined from the spectral peak of $E(f,\theta)$, whereas the mean direction characterizes the overall wave-propagation direction and is defined by Equation (12):

$$\bar{\theta} = arctan2\left(\int E(f,\theta)\sin\theta\, df d\theta\,, \int E(f,\theta)\cos\theta\, df d\theta\right) \quad (12)$$

Here, $arctan2$ denotes the two-argument arctangent function, with the signs of the integrated sine and cosine components determining the quadrant of the mean wave direction. Equation (12) adopts the "FROM" convention, in which the reported wave direction indicates the direction from which the waves arrive, with true north defined as 0°. In essence, the equation performs an energy-weighted average of the directional information across the full spectrum, yielding the mean wave direction for the sea state as a whole. For single-point, long-term observation platforms such as GNSS buoys, the mean wave direction is typically estimated within this frequency–direction spectral framework.

3.4. Accuracy Analysis

Different buoy technologies retrieve wave parameters by measuring buoy motion in response to waves. Although accelerometer-based and GNSS buoys differ markedly in their raw observables and how measurement errors are characterized, both ultimately express buoy motion in terms of displacement-equivalent quantities. To provide a common basis for comparison, this section considers the accuracy of both buoy types at three levels: raw observables, equivalent displacement and wave parameters. Representative studies are summarized in Table 8. The accuracy metrics used across studies are not uniform, and most studies focus on final wave parameters while providing limited accuracy information for intermediate motion estimates. The symbol "\" therefore indicates that the corresponding value was not reported separately in the cited study. H_s denotes significant wave height; T_m, the mean wave period; T_p, peak period; D, wave direction, including peak direction D_p and mean direction D_m. Moreover, the statistical metrics reported in Table 8 characterize measurement agreement and error behavior from complementary perspectives. The correlation coefficient (R) quantifies the strength of the linear association between two sets of observations but does not directly measure their numerical discrepancy. RMSE quantifies the overall difference between the evaluated and reference values. STD describes data dispersion, although its interpretation depends on the quantity being summarized. NRMSE normalizes RMSE by a specified reference scale, whereas relative error expresses the measurement difference as a fraction of the reference value. Bias denotes the mean difference between the evaluated and reference values. These metrics may be calculated differently across studies because of differences in error definitions, normalization procedures and the statistical quantities considered. They should therefore be interpreted in accordance with the definitions provided in the original references.

Table 8. Accuracy comparison across buoy technology pathways.

Buoy Approach	Reference	Raw-Observable Accuracy	Equivalent-Displacement Accuracy	Wave Parameter Comparison Method	Wave-Parameter Results
Accelerometer-based	[91]	75–430 $\mu g/\sqrt{Hz}$	\	Accelerometer-based buoy versus fixed wave gauge	H_s, Relative error $\leq 2\%$
Accelerometer-based	[92]	\	\	GNSS (PPK) versus accelerometer (same buoy)	H_s, RMSE $= 6.5$ cm
Velocity-based (Doppler)	[9]	\	Three-dimensional motion accuracy: 1 cm	GNSS versus accelerometer (same buoy)	H_s, $R = 0.99$; T_p, $R = 0.98$; D_p, $R = 0.99$
Displacement-based	[93]	\	\	GNSS versus accelerometer (same buoy)	H_s, $R = 0.99$, T_m, $R = 0.99$ H_s, RMSE $= 7.1$ cm T_m, RMSE $= 0.28$ s

Velocity-based (Doppler)	[21]	\	Versus prescribed displacement (wave-generation test): mean vertical-amplitude deviation = 4%	GNSS versus accelerometer (same buoy)	H_s, NRMSE = 4.2%; T_m, NRMSE = 4.4%; mean wave-direction deviation = 10.5°
Velocity-based (Doppler)	[24]	\	\	GNSS buoy versus accelerometer-based buoy (Datawell DWR-MkIII)	H_s, RMSE = 5.02 cm; T_m, RMSE = 0.22 s, wave-direction RMSE = 9.27°
Velocity-based (variometric)	[4]	3 mm/s (1 Hz; estimated vertical velocity error).	Versus PPP: vertical displacement STD = 11.0 cm	GNSS carrier-phase-based buoy versus Doppler-based GNSS buoy (Datawell DWR-G4)	H_s, RMSE = 3.4 cm; T_m, RMSE = 0.16 s
Velocity-based (TDCP)	[26]	8.8 mm/s (1 Hz; vertical STD of static L1 TDCP measurements)	Versus PPK: vertical displacement STD = 1.84 cm	GNSS TDCP versus PPK solutions	H_s, STD = 0.7 cm; T_m, STD = 0.1 s
Velocity-based (variometric)	[27]	\	Versus PPK: horizontal RMSE = 1 cm; vertical RMSE = 3 cm	GNSS variometric versus PPK solutions	H_s, RMSE = 3 cm; T_m, RMSE = 0.12 s; D, RMSE = 1.05°
Displacement-based (PPP and PPK)	[25]	PPK: 1–3 cm (vs. tide gauge); still-water noise STD: 1.8 cm.	\	GNSS PPP vs. PPK solutions	H_s, RMSE = 1.3 − 1.4 cm

Intercomparisons between GNSS buoys and conventional accelerometer-based buoys have shown that the RMSEs of H_s reported by Bender and Qi were both on the order of a few centimeters. Doong reported a normalized error of 4.2% after data processing, while the same-buoy intercomparison conducted by de Vries also showed a very high correlation. Similar behavior has been observed among different GNSS technology approaches, with H_s estimates from several studies showing overall good agreement. Although the studies used different evaluation metrics, reference instruments, frequency-processing conditions and experimental environments, making direct comparisons of accuracy difficult, further analysis of the supplementary experiments reported in the relevant literature indicates that differences in raw observation accuracy were not reflected proportionally in the final wave parameters. Liu estimated the vertical velocity errors of the variometric and Doppler methods to be approximately 31 and 186 mm/s, respectively, yet their H_s RMSEs relative to the Datawell DWR-G4 were only 3.4 and 4.1 cm. Doong found that insufficiently processed GPS data yielded an H_s correlation coefficient below 0.5, whereas outlier treatment and frequency cut-off increased the coefficient to above 0.95. Bender showed that an acceleration-based processing method with insufficient correction for attitude effects could lead to an average overestimation of H_s of approximately 26%. These results indicate that raw observation accuracy alone does not determine the consistency of the final wave parameters; data-quality control, attitude correction and spectral processing also have important effects.

Further comparison of results obtained under different validation conditions within the same study indicates that intercomparisons among processing methods applied to the same GNSS observations generally yield higher agreement than comparisons with independent buoys. For example, in Xue et al., the RMSEs of H_s and T_m between the Variometric and PPK methods were 3 cm and 0.12 s, respectively. When compared with an independent Datawell buoy, these values increased to 0.05 m and 0.75 s. The multiple intercomparison experiments by Yang and Zhu summarized in Table 8 showed a similar pattern. Under identical GNSS observation conditions, different processing methods can generally produce consistent estimates of H_s and some period parameters. This agreement should not, however, be equated directly with agreement between independent wave-

measurement systems, because the latter may also reflect differences in buoy response, mooring conditions, spatial separation, sampling conditions and errors in the reference instruments.

Existing intercomparisons of wave parameters indicate that different technology approaches generally show good agreement in H_s. By comparison, although the overall differences in period parameters remain relatively small, their stability depends on the period definition. Mean period generally remains in good agreement, whereas peak period T_p is more susceptible to deviations in multimodal spectra or when the spectral-peak location changes. Directional parameters show larger discrepancies. For example, the wave-direction differences reported by Doong and Qi were both close to 10°, and Patra found a lower correlation for total wave direction than for H_s. The agreement improved substantially after wind sea and swell were separated.

To understand the agreement in wave parameters across different technology approaches, it is first necessary to examine the transformation relationships linking their raw motion observables. Accelerometer-based, GNSS velocity-based and GNSS displacement-based buoys measure acceleration $a(t)$, velocity $v(t)$ and displacement $\eta(t)$, respectively. These quantities describe different orders of wave-induced buoy motion and are related by Equations (13) and (14):

$$v(t) = \frac{d\eta(t)}{dt} \tag{13}$$

$$a(t) = \frac{d^2\eta(t)}{dt^2} \tag{14}$$

In the frequency domain, with angular frequency $\omega = 2\pi f$, the velocity and acceleration spectra can each be converted into a sea-surface displacement spectrum according to Equations (15) and (16), respectively:

$$S_\eta(f) = \frac{S_v(f)}{(2\pi f)^2} \tag{15}$$

$$S_\eta(f) = \frac{S_a(f)}{(2\pi f)^4} \tag{16}$$

Here, $S_\eta(f)$, $S_v(f)$ and $S_a(f)$ are the displacement, velocity and acceleration power spectra, respectively. Displacement-based GNSS buoys estimate $S_\eta(f)$ directly from displacement time series, placing all three approaches on a common basis: the sea-surface displacement spectrum. More importantly, the above relationships determine how observation errors are transferred across frequency. In terms of power-spectral density, velocity noise contributes to the displacement spectrum with an f^{-2} weighting, whereas acceleration noise is weighted by f^{-4}. Equation (5) explicitly quantifies the contribution of velocity-measurement errors to the additional noise in the reconstructed displacement spectrum. Direct displacement measurements, by contrast, are not subject to this integration-induced frequency weighting. Their absolute-positioning errors may nevertheless contain static biases and low-frequency drift, which cannot be directly equated with dynamic-displacement errors within the target wave-frequency band.

For wave parameters derived from spectral moments, errors in the displacement spectrum first propagate into each spectral moment through frequency-weighted integration. This relationship is expressed by Equation (17).

$$\delta m_n = \int_{f_l}^{f_h} f^n \delta S_\eta(f)\, df \tag{17}$$

Here, δm_n denotes the error in the spectral moment of order n, $\delta S_\eta(f)$ denotes the difference between the reconstructed and true displacement spectra and f_l and f_h are the lower and upper frequency limits used in the spectral-moment calculation, respectively. Observation errors therefore propagate through a sequence of stages: conversion

from the raw observations to the displacement spectrum, integration of displacement-spectrum errors into spectral-moment errors and propagation of spectral-moment errors into the derived wave parameters. Errors in the displacement spectrum, however, are not transferred proportionally to significant wave height. Their effect depends mainly on the frequency range in which they occur and on their contribution to the total spectral energy within the target wave band. Under linear random wave theory, significant wave height is defined by Equation (6), and first-order error propagation yields Equation (18).

$$\frac{\delta H_s}{H_s} \approx \frac{\delta m_0}{2m_0} \approx \frac{1}{2m_0}\int_{f_l}^{f_h} \delta S_\eta(f)df \tag{18}$$

Here, $\delta S_\eta(f)$ is the displacement-spectrum error, and f_l and f_h define the frequency band used for wave-parameter estimation. A local spectral error affects H_s through its contribution to the integrated energy, and hence to the zeroth spectral moment m_0, rather than through its amplitude at a single frequency. An error confined to a narrow band with little contribution to the total energy therefore has a limited effect on H_s. Because H_s scales with $\sqrt{m_0}$, first-order propagation under small perturbations also halves the relative error transferred from m_0 to H_s. High-pass or band-pass filtering further limits the frequencies entering the integral, so low-frequency positioning drift and integration-induced noise need not contribute fully to the final estimate. Accordingly, if different technology approaches recover the spectral energy within the dominant wave-frequency band with sufficient fidelity, while residual spectral errors contribute only modestly to the zeroth spectral moment, their retrieved significant wave heights may still agree well despite differences in raw-observation accuracy and local spectral errors.

Mean wave periods depend on combinations of spectral moments. For T_{m02}, first-order error propagation yields Equation (19):

$$\frac{\delta T_{m02}}{T_{m02}} \approx \frac{1}{2}\left(\frac{\delta m_0}{m_0} - \frac{\delta m_2}{m_2}\right) \tag{19}$$

The corresponding error in the second spectral moment, δm_2, is given by Equation (20):

$$\delta m_2 = \int_{f_l}^{f_h} f^2 \delta S_\eta(f)df \tag{20}$$

Whereas m_0 applies no additional frequency weighting, the f^2 factor in m_2 increases the contribution of high-frequency spectral errors. Errors in the spectral tail may therefore have little effect on total energy or H_s but a greater effect on the mean period through m_2. Consistent with this, Xue et al. reported a mean-period difference of approximately 0.28 s between sampling rates of 1.28 and 5 Hz while holding the input JONSWAP spectrum fixed and attributed it to high-frequency contributions to the period estimate. Mean periods nevertheless integrate information across the frequency band and are generally less affected by isolated spectral perturbations than T_p, which depends on the location of the largest peak. When a spectrum has multiple peaks of comparable energy, modest observation noise or differences in frequency resolution or spectral estimation can change the identified dominant peak, producing a larger difference in T_p.

Directional estimates show larger discrepancies because they depend on both spectral energy and the correlation and phase relationships between horizontal and vertical motion components. A first-order approximation to the error in mean wave direction is given by Equation (21):

$$\delta D_m \approx \frac{a_1\delta b_1 - b_1\delta a_1}{a_1^2 + b_1^2} \tag{21}$$

Here, a_1 and b_1 are the first-order cosine and sine moments of the directional distribution (Equation (12)). Because mean wave direction depends on their relative values, it is sensitive not only to spectral-energy errors but also to the redistribution of energy across directions. Directionally concentrated waves have a larger $a_1^2 + b_1^2$ and a more

stable direction estimate. With broader spreading or multiple wave systems, contributions to the directional moments may partially cancel, reducing $a_1^2 + b_1^2$ and amplifying the directional response to a given spectral perturbation. Consequently, similar total spectral energy across measurement approaches does not guarantee similar mean wave directions if horizontal motion, phase relationships or directional energy distributions differ. This greater sensitivity helps explain why directional parameters often agree less closely than H_s and mean period.

The retrieval accuracy of long-period swell is jointly controlled by low-frequency noise and the filtering strategy. If low-frequency noise is not adequately suppressed, its amplification in the displacement spectrum can lead to an overestimation of spectral energy within the swell band and affect swell height and mean period through the zeroth and negative-first spectral moments. If a spurious low-frequency peak exceeds the true spectral peak, the peak period may also be misidentified. Increasing the high-pass cutoff frequency can reduce low-frequency noise but may also attenuate genuine long-period swell signals. This can cause the swell spectral energy and corresponding wave height to be underestimated and may even alter the identified spectral peak. Low-frequency filtering should therefore be understood as a trade-off between suppressing spurious spectral energy and preserving genuine long-period signals, rather than as a simple noise-removal procedure. Consequently, even when different technology approaches yield similar overall significant wave heights, their retrievals of long-period swell may differ substantially because of differences in low-frequency noise and filter settings.

4. Representative GNSS Wave-Buoy Systems and Their Applications

4.1. Representative GNSS Wave Buoys

GNSS wave buoys have evolved into operational platforms capable of onboard processing, real-time telemetry and long-duration deployment. Representative systems include DWR-G, Spotter and microSWIFT. Developed by Datawell, the DWR-G uses a single GPS receiver to measure three-dimensional velocity and reconstruct displacement through integration, without requiring a shore-based reference station or routine calibration. It samples at 1.28 Hz, covers wave periods of 1.6–100 s and provides a three-axis measurement accuracy of approximately 0.01–0.02 m under freely floating conditions. Its spectral range is 0.025–0.60 Hz, with outputs including three-dimensional displacement, wave spectra, wave direction and buoy position. The system represents a mature implementation of GNSS velocity measurement for long-term wave observation (Figure 4a). Spotter, developed by Sofar Ocean, is a compact operational GNSS wave buoy powered by solar energy and equipped with iridium and cellular communications (Figure 4b). It weighs less than 5.5 kg, records three-dimensional displacement at 2.5 Hz and provides wave spectra over 0.03–0.8 Hz. Spectrally derived parameters include significant wave height, wave period and mean wave direction, with field measurements generally differing from those of the DWR-G4 by less than 10% [31]. Developed by the University of Washington, microSWIFT combines low cost with onboard processing and telemetry. The v1 system uses a Raspberry Pi Zero processor and costs no more than US$600 per unit. Its significant wave-height measurements agree with those from a Datawell Waverider to within ±0.1 m. During hurricanes, microSWIFT and Spotter also produced broadly consistent frequency and directional spectra for significant wave heights of 2.7–7.4 m [32]. The subsequent v2 system uses a low-power STM32 microcontroller, extends operational endurance to 30 days, and supports deployment from aircraft (Figure 4c). This expendable buoy costs approximately US$900 per unit and can optionally carry temperature and salinity sensors in addition to providing wave spectra and standard wave parameters.

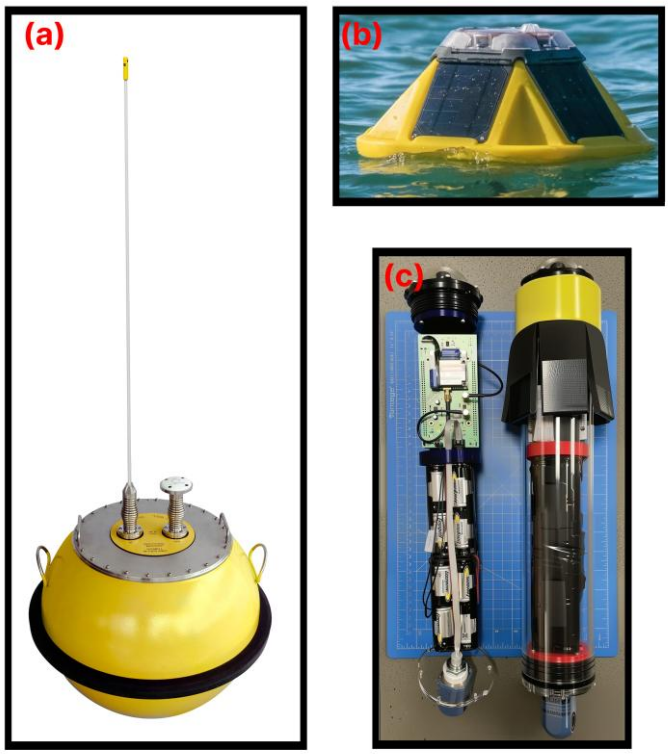


Figure 4. Representative GNSS wave buoys. Panel (**a**) is sourced from the official Datawell website (https://datawell.nl/), panel (**b**) is reproduced from [31] and panel (**c**) is reproduced from [32].

4.2. Publicly Available Data

Major operational buoy networks, including the National Data Buoy Center (NDBC) and the Coastal Data Information Program (CDIP), remain dominated by accelerometer-based systems, with GNSS buoys contributing observations at only a limited number of stations. By contrast, the Nationwide Ocean Wave Information Network for Ports and Harbours (NOWPHAS) has incorporated GNSS buoys into its monitoring network since 2007, and they have become an important component of wave observation around Japan. Eighteen GNSS buoy stations are distributed across coastal ports and offshore waters (Figure 5), typically 10–20 km offshore at water depths of 100–400 m. Publicly available records include significant wave height, significant wave period and wave direction.

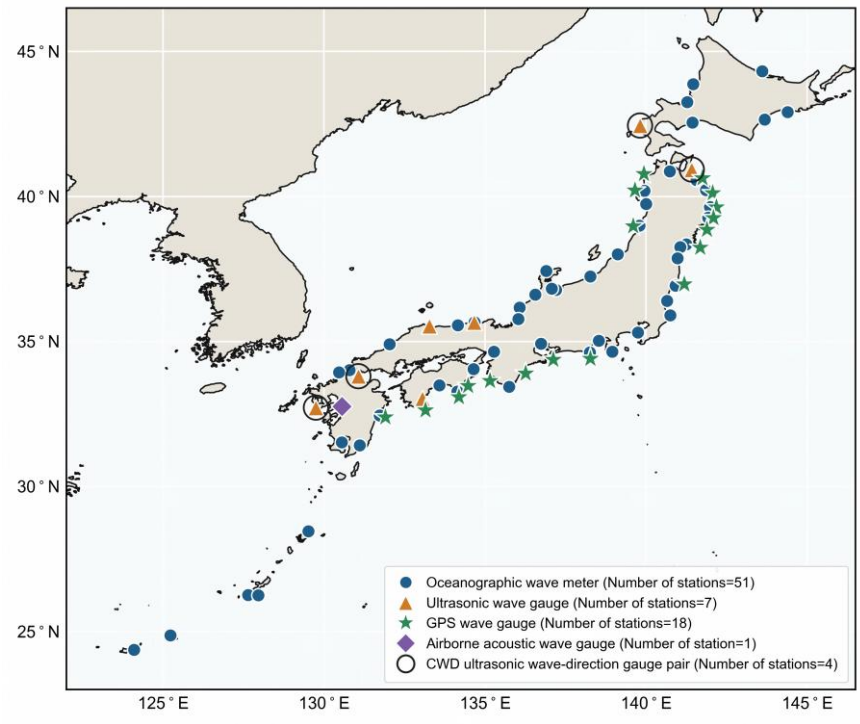


Figure 5. Spatial distribution of NOWPHAS wave-observation stations by instrument type in 2024.

The Sofar Spotter Archive is a global historical dataset released by Sofar Ocean, providing wave and wind observations from the Spotter buoy network. It contains more than seven million hours of sea-surface observations collected between 2019 and March 2022 across open-ocean and nearshore waters. The archive supports wave-model validation, satellite-product validation, wave-data assimilation and global wave-climate analysis. Figure 6 maps the Spotter buoy locations on 4 March 2022 and the corresponding significant wave heights.

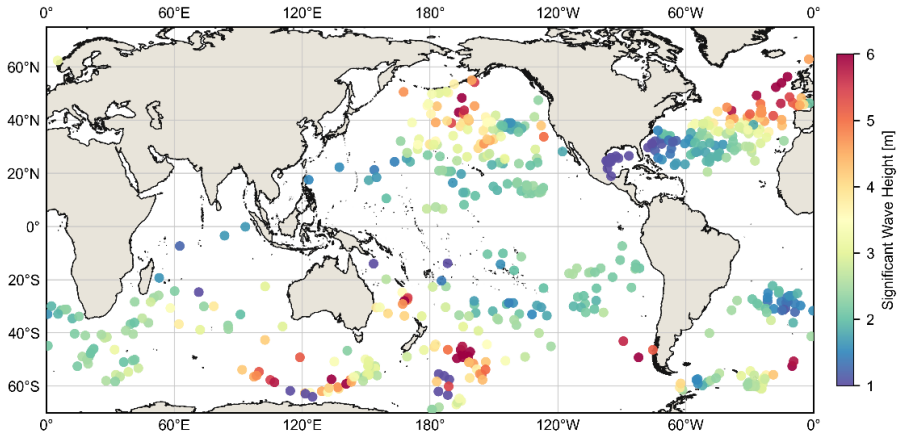


Figure 6. Spatial distribution of Spotter buoys and the corresponding significant wave heights on 4 March 2022.

Australia's Integrated Marine Observing System (IMOS) operates a coastal wave-buoy array and the public AusWaves data platform, which provides real-time and historical observations from Australian coastal waters. These data support wave-forecast validation, coastal-hazard assessment, marine engineering and related applications. The network relies primarily on Spotter buoys, most of which are moored in nearshore waters 15–80 m deep, together with a smaller number of drifting platforms. In total, the network comprises approximately 60 observing units, whose locations are summarized in Figure

7. Public data products include buoy position, wave parameters and frequency spectra; selected buoys also measure wind speed, wind direction and water temperature.

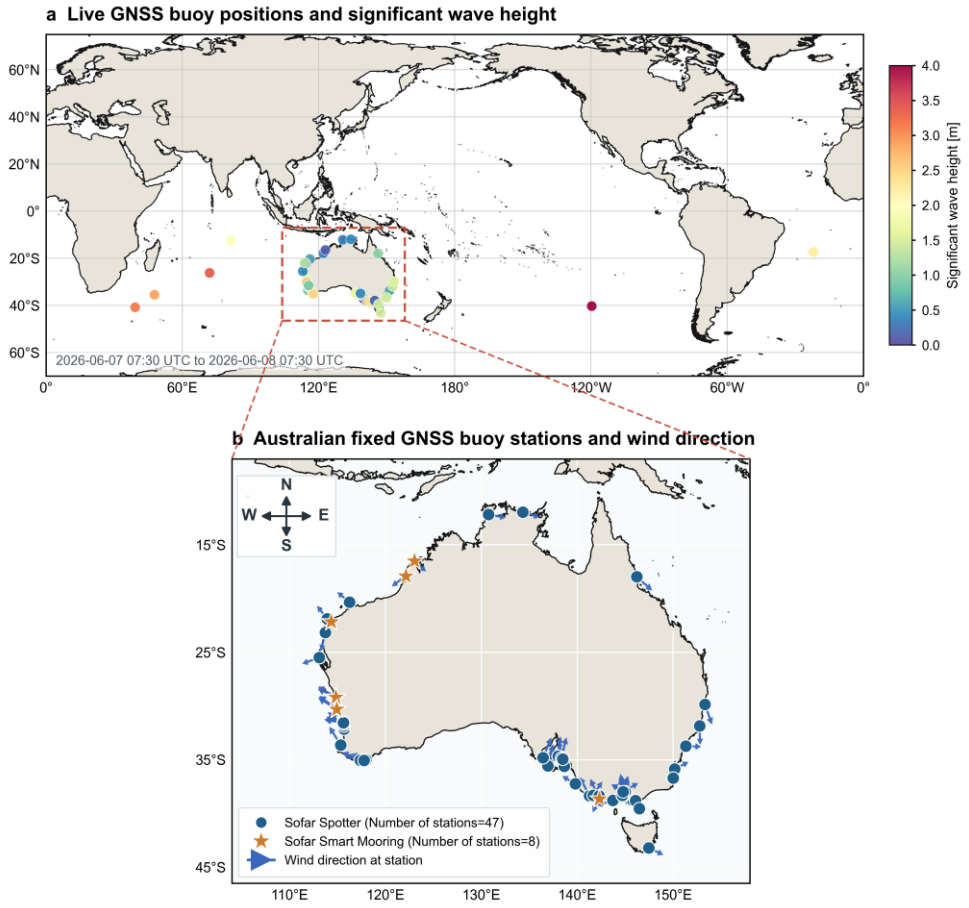


Figure 7. Buoy locations and selected observations on 7 June 2026. (**a**) Locations of active buoys and the corresponding significant wave heights. (**b**) Locations of moored buoys along the Australian coast and the corresponding wind directions.

The microSWIFT data collection, released by Thomson, is an open research dataset of observations from compact expendable GNSS wave buoys (Figure 8). It covers several field campaigns conducted between 2022 and 2025 in environments including the Arctic Ocean, hurricane conditions, and the Atlantic Ocean. Alongside buoy positions, wave parameters and frequency spectra, the dataset includes measurements of salinity and temperature. These records support studies of extreme storms, wave propagation through sea ice, wave–current interactions and validation of modeled wave spectra. Data coverage is heterogeneous across campaigns, with substantial differences in deployment location, buoy number and record length.

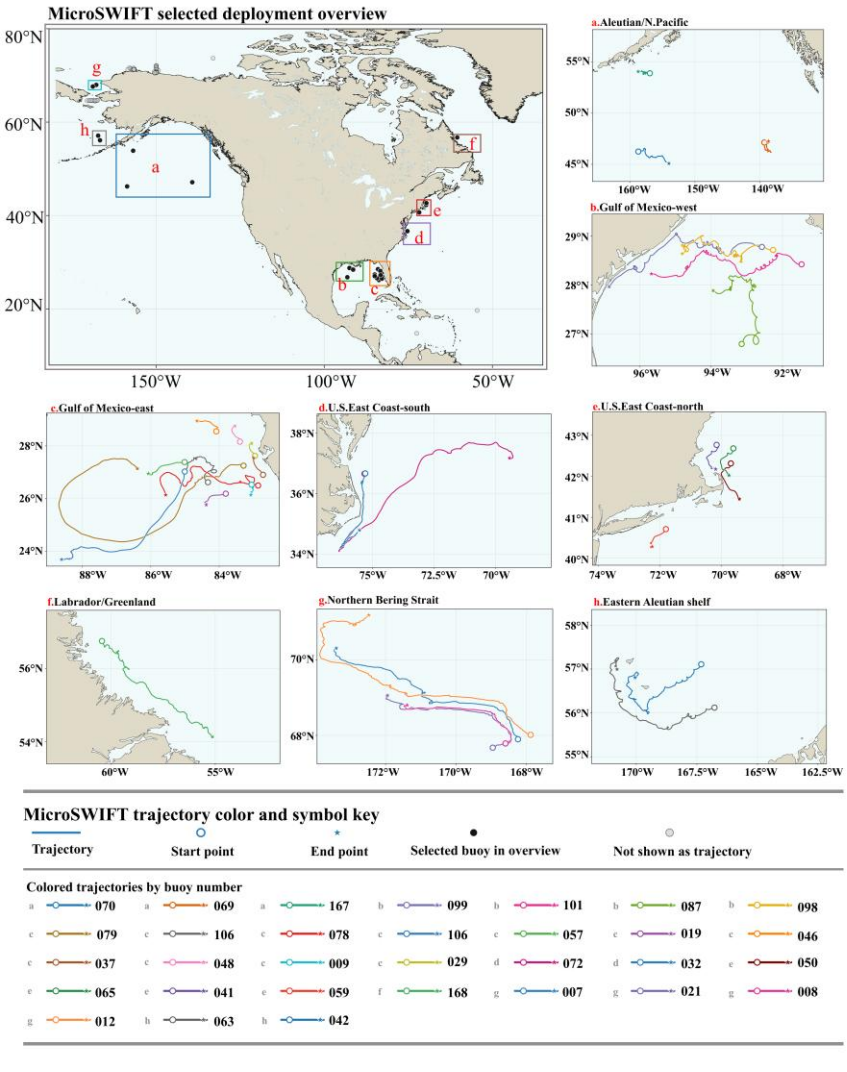


Figure 8. Locations and regional trajectories of microSWIFT buoys. (**a**–**h**) Buoy trajectories within the corresponding regions.

Analysis of publicly available datasets shows that GNSS buoys have yet to become the dominant platforms in established operational networks. These networks already rely on stable instrument configurations, mature quality-control procedures and long-term observational records. Replacing existing systems would increase deployment and maintenance costs and could disrupt data consistency and continuity. AusWaves illustrates the regional-network model, with most GNSS buoys deployed in coastal waters. By contrast, the Sofar Spotter Archive and microSWIFT datasets demonstrate the potential of compact GNSS buoys for globally distributed observations. GNSS buoys therefore currently complement rather than replace conventional accelerometer-based systems. Their role is likely to expand through progressive integration into existing networks and the development of new observing networks centered on GNSS platforms.

4.3. Advances in Applications

GNSS wave buoys offer a new approach to in situ monitoring under complex sea conditions. Early applications focused on moored, fixed-point observations in nearshore waters, providing wave parameters for marine engineering and related needs. Nearshore trials have also served as testbeds for assessing how GNSS measurement methods and processing strategies affect wave-parameter retrieval. In the open ocean, drifting GNSS buoys simultaneously record wave parameters and drift trajectories, providing field data

on wind-sea development, swell propagation and wave–current interactions. Representative systems, including Spotter and MicroSWIFT, have been deployed in open-ocean campaigns from ships or aircraft.

GNSS buoys also provide in situ reference measurements for satellite-altimeter calibration and validation. During satellite overpasses, buoy-derived instantaneous sea-surface heights are collocated in space and time with altimeter estimates, while concurrent wave parameters and spectra are used to assess satellite-derived wave products. GNSS buoys have supported calibration and validation for the TOPEX/Poseidon, Jason-1, Jason-2, Sentinel-6, and SWOT missions [94–97]. Deployments have expanded from single-site comparisons to multi-buoy arrays spanning up to 80 km [98].

GNSS wave buoys provide independent in situ constraints for validating numerical wave models. Spotter observations have been used to evaluate SWAN simulations and ERA5 reanalysis data, with significant wave-height correlations of 0.89 and 0.92, respectively, although agreement was weaker for wave direction [99,100]. Smit et al. further assimilated significant wave heights from a drifting Spotter network in the North Pacific into a WAVEWATCH III-based global forecasting system. Assimilation reduced the overall significant wave-height RMSE by 27% and, for an intense swell event, reduced errors in arrival time and wave height by approximately 6 h and 1 m, respectively [3]. GNSS wave buoys therefore support both model evaluation and data assimilation, providing a direct pathway from in situ observation to improved wave-forecast skill.

Miniaturization and cost reduction are prominent trends in the development of GNSS wave buoys. Miniaturization is enabled by integrating GNSS receivers, low-power microcontrollers and satellite-communication modules, while commercial off-the-shelf components and 3D printing reduce electronic and structural costs, respectively [101]. Float geometry reflects the intended observation strategy. Spherical buoys are designed to follow water-particle orbital motion (Figure 9a), whereas disc-shaped platforms provide greater capacity for integrating GNSS receivers and other sensors (Figure 9b). Attitude-assisted designs additionally use buoy-attitude measurements to correct antenna-height errors or quantify uncertainty in retrieved wave parameters (Figure 9c). GNSS measurements have also been extended beyond conventional buoy platforms. Hole et al., for example, integrated a GNSS receiver into an uncrewed surface vehicle and obtained reliable wave observations (Figure 9d) [102].

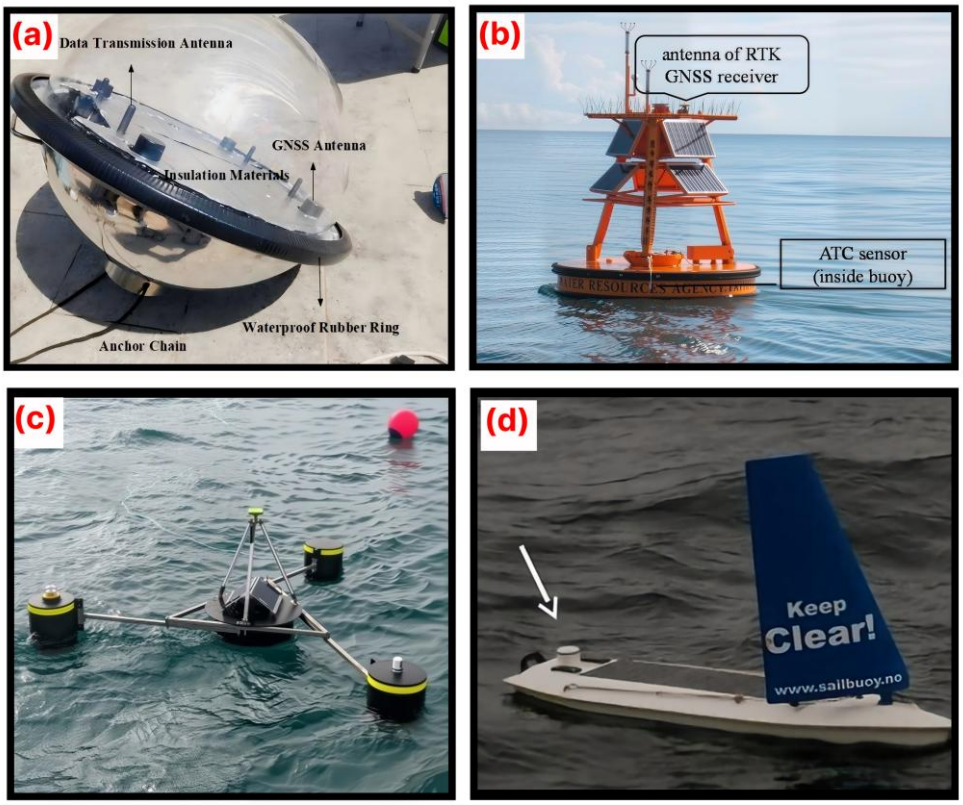


Figure 9. Representative structural configurations of GNSS wave buoys. (**a**–**d**), Images reproduced from [101], [42], [98] and [102], respectively. The non-English text on the buoy in panel (**b**) identifies the organization to which the buoy belongs.

Spherical designs remain common among GNSS buoys (Figure 9). Their wave-following characteristics underpin established systems such as DWR-G and Spotter, but smaller, more integrated GNSS instruments are extending wave measurements to microSWIFT, navigation buoys and uncrewed surface platforms. These platforms differ in size, mass, geometry and mooring and therefore need not respond identically to sea-surface motion. Nevertheless, such differences have not consistently produced comparable differences in retrieved wave parameters. Jensen et al. compared two structurally distinct platforms differing approximately 23-fold in mass and reported an H_s RMSE of approximately 0.30 m; for H_s below approximately 7 m, most differences were within 0.25 m [103]. Saetre et al. found no marked change in H_s or wave-direction accuracy after altering a navigation buoy's mooring and adding approximately 30 kg [104]. Similarly, long-term biofouling changed a Waverider's mass and hydrodynamic response but mainly attenuated its high-frequency response, with only a small effect on wave parameters [105]. The influence of platform design on wave-measurement performance therefore merits closer examination as GNSS observations expand beyond dedicated buoys; Section 5.2 discusses this issue.

5. Discussion

5.1. Assessing GNSS Wave-Buoy Accuracy at Different Levels

Although various GNSS wave-buoy approaches have been validated and compared, studies differ in sea state, reference measurements, frequency range and accuracy metrics. They also report final wave parameters more often than the accuracy of intermediate motion estimates. The available results therefore characterize performance under particular test conditions but do not support a consistent accuracy ranking across approaches.

All GNSS buoy approaches aim to reconstruct wave-induced buoy motion, making dynamic displacement accuracy within the target wave band a useful common basis for comparison. Position, velocity and carrier-phase measurements are not directly comparable as raw observables. Expressing each as band-limited dynamic displacement or a displacement spectrum better captures motion-reconstruction accuracy and exposes differences that may be masked by the spectral integration used to derive final wave parameters. Target-band dynamic displacement should therefore be retained as an intermediate assessment level between raw GNSS observations and derived wave parameters.

Accuracy assessment of dynamic displacement within the target frequency band should account for the effect of filtering on the effective observational bandwidth, particularly in the low-frequency region occupied by long-period swell. Even when different buoys use the same spectral-moment calculation method, differences in high-pass cutoff frequency, transition-band characteristics and noise-suppression strategy can lead to different levels of recovery of low-frequency spectral energy. Accordingly, evaluating long-period swell should involve more than a comparison of overall significant wave height. It should also consider low-frequency spectral agreement, swell-partitioned wave height and period parameters, while explicitly reporting the cutoff frequency, effective passband and spectral integration range used by each system.

A single accuracy metric cannot establish an absolute ranking while test conditions remain inconsistent. Although individual studies identify methods with higher motion-reconstruction accuracy under specific conditions, the approaches also differ in real-time capability, reliance on reference stations or precise GNSS products and computational and communication demands. To improve the comparability of accuracy assessments across different technology approaches, wave-measurement accuracy should be validated sequentially at three levels: raw observations, equivalent displacement and wave parameters. First, the accuracy of the raw observations should be assessed against controlled experiments or independent measurements. Second, observations obtained using different technology approaches should be represented on a common basis as dynamic displacement and displacement spectra within the target wave-frequency band, allowing their reconstruction accuracy to be evaluated. Finally, under consistent time windows, effective frequency bands and spectral-processing procedures, the wave spectra and key wave parameters should be compared with those obtained from independent reference instruments using the same accuracy metrics. The reference instruments, platform characteristics and sea-state conditions should also be reported explicitly so that the effects of the observation method can be distinguished from those of the experimental environment.

5.2. Practical Effects of Platform Differences on Buoy Wave-Measurement Performance

For wave-following buoys, platform-specific differences are first manifested in the frequency response of the buoy motion relative to the true sea-surface motion. This response can be described by the platform frequency-response function $R(f)$. Let $X_b(f)$ denote the buoy motion and $\eta(f)$ the true sea-surface motion. The response function can then be written in general form as Equation (22):

$$R(f) = \frac{X_b(f)}{\eta(f)} \tag{22}$$

Under the linear-response assumption, the relationship between the buoy heave-motion spectrum and the true wave spectrum can be expressed as Equation (23):

$$E_b(f) = |R(f)|^2 E_\eta(f) \tag{23}$$

Here, $E_b(f)$ denotes the energy spectrum of the buoy's vertical motion, $E_\eta(f)$ denotes the energy spectrum of the true sea-surface elevation and $R(f)$ represents the response function of the buoy's vertical motion relative to the sea-surface elevation. This

relationship shows that platform response does not affect the wave spectrum uniformly. Rather, the response amplitude at each frequency modifies the spectral energy within the corresponding frequency band.

The frequency dependence of platform response arises primarily from the buoy's hydrodynamic properties. As frequency changes, so does the balance among inertial effects, restoring forces, damping and wave forcing, leading to frequency-dependent response amplitudes. The heave natural frequency governs the platform's resonance behavior, whereas the buoy dimensions and their relation to wavelength constrain its ability to follow short, high-frequency waves. For example, to enhance wave-following performance within the target band, microSWIFT was designed with a heave natural frequency above the dominant ocean-wave energy band of 0.05–0.5 Hz. The heave natural frequency estimated for the Spotter buoy is approximately 1.2 Hz, also above the dominant wave-frequency range [31,32].

A natural frequency above the target wave band, however, does not imply a response amplitude close to unity throughout that band. Geometric factors, including buoy size, may still limit the response to short waves. Tank experiments by Hope et al. showed that the SFY buoy, with a characteristic width of approximately 15.5 cm, began to exhibit pronounced spectral-energy attenuation at around 2.2 Hz. This frequency was broadly consistent with the geometric cutoff frequency estimated from the buoy dimensions, suggesting that wave-following capability can deteriorate substantially when the wavelength approaches the buoy size [106]. Waseda further reported that the heave response of the K-TRITON test buoy remained close to ideal over 0.05–0.2 Hz, whereas pitch and roll resonances produced an anomalous peak in the horizontal-motion spectrum at approximately 0.36 Hz. These findings show that frequency- and motion-mode-dependent responses can substantially modify the buoy motion spectrum [18].

Changes in spectral energy induced by the platform frequency response can propagate into the derived wave parameters. For H_s, spectral attenuation or amplification modifies the zeroth spectral moment m_0, with the magnitude of the resulting effect determined by the fraction of total energy contained in the affected frequency band. For period parameters, attenuation of high-frequency energy may disproportionately affect the second spectral moment m_2, leading to bias in T_{m02}. Conversely, localized amplification in the platform response may shift the dominant spectral peak and thereby alter the peak period T_p. Differences in response amplitude and phase among the different motion degrees of freedom may also modify the cross-spectral relationships, thereby affecting estimates of wave direction and directional spreading.

GNSS measurement errors and platform-response biases should be distinguished according to the reference quantity against which they are evaluated. GNSS measurement error refers to the deviation between the GNSS-derived and actual buoy motion, whereas platform-response bias refers to the deviation between buoy motion and the true motion of the sea surface. In a simplified mathematical framework, platform response affects the representation of the true wave signal through a frequency-dependent transfer function. GNSS measurement error, by contrast, enters the buoy-motion observation sequence primarily as a measurement error. These two error sources also have different signatures. Platform-response bias is typically manifested as frequency-dependent attenuation or amplification of motion amplitude and phase shifts, whereas GNSS measurement error may appear as observational bias, low-frequency drift or additive noise. GNSS measurement error can therefore be evaluated using controlled-motion experiments or an independent motion reference installed on the same platform, by examining its deviation from the reference motion and its frequency distribution. Platform-response bias can be evaluated through hydrodynamic analysis or synchronized wave experiments, using the true sea-

surface motion as the reference to quantify the buoy response amplitude and phase across frequencies.

Frequency-dependent platform response does not, by itself, require explicit transfer-function correction for every buoy. Benetazzo et al. used a field-calibrated response amplitude operator (RAO) to correct a large buoy's response. By contrast, the cited studies of Spotter, microSWIFT and some navigation buoys did not apply RAO corrections to wave parameters; they relied instead on designs that place the natural frequency outside the main wave-energy band, together with frequency-band limits and quality control [31,104,107,108]. Thomson et al. reported wave-parameter errors within approximately 5% for a Wave Glider platform without establishing a transfer function. Explicit RAO correction is thus one means of managing platform response, not a universal requirement [108]. Reliable wave measurements may also be obtained through platform design and frequency-band control when the dominant wave energy falls within a stable-response range.

Overall, current evidence suggests that platform differences chiefly alter the frequency range over which buoy motion reliably represents sea-surface motion. Their effect on conventional wave parameters depends on whether the dominant wave energy lies within that range. Where long-period swell dominates and little energy occupies the affected high-frequency band, bulk parameters may remain stable despite substantial differences in high-frequency response. By contrast, platform effects may become more pronounced for short-period wind waves, high-frequency spectral analyses, extreme sea states or when a platform's natural frequency overlaps the main wave-energy band.

5.3. Suitability of Buoys as Validation References

Buoys provide key in situ references for validating satellite observations and wave models, but neither conventional nor GNSS buoys are free from measurement bias across all frequencies, parameters and observing conditions. Disagreement with a satellite product or model therefore does not, on its own, identify the product or model as erroneous. Buoy observations are better treated as reference measurements with defined error limits and conditions of use, rather than as absolute ground truth.

Disagreement can arise even when both the buoy and the dataset under validation appear reliable, because they may differ in physical definition or in the scales they represent. A mismatch between FROM and TO wave-direction conventions, for example, produces an approximately 180° offset; SAR can also have a separate 180° directional ambiguity. Buoy statistics calculated over a time window are likewise not directly equivalent to an instantaneous spatial satellite observation or a model grid-cell average. During rapidly evolving conditions, such as a typhoon, substantial changes within the window may violate the stationarity assumption and weaken the reliability of estimated wave parameters. Different observing systems represent the sea state over different spatial and temporal supports. Satellite products describe wave conditions at a particular overpass time and across a defined spatial footprint, numerical models represent wave fields at the grid scale, and buoys typically provide statistical wave parameters at a local site over a specified time window. Even after spatiotemporal collocation, these differences can introduce additional biases when the sea state evolves rapidly or exhibits substantial spatial heterogeneity.

The suitability of a GNSS buoy as a validation reference therefore depends on both the reliability of its observations and the degree to which the two datasets share comparable physical definitions and spatiotemporal representativeness. In practical validation, collocation criteria should be selected carefully to minimize the influence of differences in sampling scales. When buoy observations are reliable and well matched to the data being evaluated in terms of physical definition and observation scale, they can provide a high-confidence in situ reference. For isolated cases of disagreement, consistency should be assessed in conjunction with observations from multiple independent sources.

6. Conclusions

This review synthesizes the measurement principles, wave-parameter retrieval methods, representative systems and applications of GNSS wave buoys. It traces the technical pathway from acquiring observations and estimating buoy motion to retrieving wave parameters and applying the resulting data. The main conclusions are as follows:

1. GNSS wave-observation approaches differ chiefly in how buoy motion is measured. Displacement-based methods directly obtain sea-surface displacement time series; among these, DGNSS, PPK and RTK are better suited to nearshore observation. Velocity-based methods generally operate without shore-based reference stations and offer considerable potential for autonomous, large-scale observation in the open ocean.
2. The studies reviewed here indicate that within the sea-state and frequency ranges examined, significant wave heights derived from GNSS and accelerometer-based measurements on the same buoy generally showed good agreement, with high correlation coefficients ($R = 0.99$) and low RMSE values (≤7.1 cm). Other intercomparison studies using independent reference buoys also reported relatively small discrepancies in significant wave height and mean period in some cases (H_s RMSE ≤ 5.02 cm, $T_m RMSE \leq 0.22$ s). In contrast, wave-direction estimates may exhibit relatively large angular deviations in some studies ($RMSE \leq 9.27°$). Nevertheless, because the evaluation metrics and reference instruments varied across studies, these results should not be extrapolated beyond the tested sea states and observation systems.
3. Mature GNSS wave-buoy systems, including DWR-G, Spotter and microSWIFT, now support both fixed-site and drifting observations. Publicly available research data show that although they have not fully replaced accelerometer-based buoys, GNSS buoys are widely used for in situ monitoring, satellite-observation validation, wave-model evaluation and oceanographic data assimilation. Their development is moving towards smaller, lower-cost systems integrated across multiple platforms.
4. GNSS buoy performance varies with frequency and application context, so a single accuracy metric cannot capture the practical performance of different approaches and platforms. Evaluation should consider motion reconstruction in the target wave band, platform response and application conditions alongside final wave parameters. When used as external validation references, GNSS buoys also require consideration of observational comparability when attributing errors.

GNSS buoy performance remains limited by GNSS signal-reception quality, while directional-spectrum retrieval in complex sea states and long-term operational performance need further improvement. Continuing advances in GNSS technology will enhance buoy observation and engineering capabilities, enabling larger-scale deployment and broader applications. Open-ocean systems will become smaller and lighter; nearshore systems should incorporate tidal-level observations and develop towards high-accuracy, networked continuous monitoring. Improved data standards, evaluation frameworks and retrieval reliability may ultimately make GNSS wave buoys core nodes of the marine in situ observing system.

Author Contributions: Conceptualization, A.Z. and K.M.; methodology, A.Z. and K.M.; software, A.Z.; validation, A.Z., K.M., M.L. and D.W.; formal analysis, A.Z. and D.W.; investigation, A.Z. and D.W.; resources, K.M. and M.L.; data curation, A.Z.; writing—original draft preparation, A.Z.; writing—review and editing, A.Z., K.M., D.W. and M.L.; visualization, A.Z.; supervision, K.M. and M.L.; project administration, K.M.; funding acquisition, K.M. and X.C. All authors have read and agreed to the published version of the manuscript.

Funding: This research was funded by the National Natural Science Foundation of China (grant number 72501293). The APC was funded by the National Natural Science Foundation of China.

Data Availability Statement: The datasets used in this study are publicly available. Spotter buoy data were obtained from the Sofar Spotter Archive (https://registry.opendata.aws/sofar-spotter-archive (accessed on 15 May 2026), AusWaves product data from https://auswaves.org/ and micro-SWIFT data from the Dryad data repository (https://doi.org/10.5061/dryad.jdfn2z3j1 (accessed on 15 May 2026).

Conflicts of Interest: The authors declare no conflicts of interest.

References

1. Holthuijsen, L.H. *Waves in Oceanic and Coastal Waters*; Cambridge University Press: Cambridge, UK, 2010.
2. Herbers, T.; Jessen, P.; Janssen, T.; Colbert, D.; MacMahan, J. Observing ocean surface waves with GPS-tracked buoys. *J. Atmos. Ocean. Technol.* **2012**, *29*, 944–959.
3. Smit, P.; Houghton, I.; Jordanova, K.; Portwood, T.; Shapiro, E.; Clark, D.; Sosa, M.; Janssen, T. Assimilation of significant wave height from distributed ocean wave sensors. *Ocean Model.* **2021**, *159*, 101738.
4. Liu, Y.; Li, M.; Liu, Y.; Wang, Y.; Jiang, S.; Wang, Y.; Tian, L.; Qiao, F. Real-time precise measurements of ocean surface waves using GNSS variometric approach. *Int. J. Appl. Earth Obs. Geoinf.* **2022**, *115*, 103125.
5. DeLoach, S.R. *GPS Tides: A Project to Determine Tidal Datums with the Global Positioning System*; US Army Corps of Engineers, Topographic Engineering Center: Alexandra, VA, USA, 1995.
6. Kato, T.; Terada, Y.; Kinoshita, M.; Kakimoto, H.; Isshiki, H.; Matsuishi, M.; Yokoyama, A.; Tanno, T. Real-time observation of tsunami by RTK-GPS. *Earth Planets Space* **2000**, *52*, 841–845.
7. Kato, T.; Terada, Y.; Kinoshita, M.; Kakimoto, H.; Isshiki, H.; Moriguchi, T.; Takada, M.; Tanno, T.; Kanzaki, M.; Johnson, J. A new tsunami monitoring system using RTK-GPS. In Proceedings of the International Tsunami Symposium, Seattle, WA, USA, 7–10 August 2001.
8. Nagai, T.; Satomi, S.; Terada, Y.; Kato, T.; Nukada, K.; Kudaka, M. GPS buoy and seabed installed wave gauge application to offshore tsunami observation. In Proceedings of the ISOPE International Ocean and Polar Engineering Conference, Seoul, South Korea, 19–24 June 2005; pp. ISOPE-I-05-282.
9. De Vries, J.; Waldron, J.; Cunningham, V. Field tests of the new Datawell DWR-G GPA wave buoy. *Sea Technol.* **2003**, *44*, 50–55.
10. Lin, Y. Development and Applications of a GNSS Buoy for Monitoring Tides and Ocean Waves in Coastal Areas. Ph.D. Thesis, National Cheng Kung University, Tainan, Taiwan, 2018.
11. Bender III, L.; Howden, S.; Dodd, D.; Guinasso Jr, N. Wave heights during Hurricane Katrina: An evaluation of PPP and PPK measurements of the vertical displacement of the GPS antenna. *J. Atmos. Ocean. Technol.* **2010**, *27*, 1760–1768.
12. Kuo, C.-Y.; Chiu, K.-W.; Chiang, K.-W.; Cheng, K.-C.; Lin, L.-C.; Tseng, H.-Z.; Chu, F.-Y.; Lan, W.-H.; Lin, H.-T. High-frequency sea level variations observed by GPS buoys using precise point positioning technique. *TAO Terr. Atmos. Ocean. Sci.* **2012**, *23*, 209.
13. Shan, R.; Cheng, X.; Yang, H.; Lu, K.; Mei, S.; Dong, L. Tide and Wave Measurement Application Researches Based on GNSS Technology. In Proceedings of the EGU General Assembly Conference Abstracts, Vienna, Austria, 8–13 April 2018; p. 3231.
14. Shan, R.; Cheng, X.; Zhou, T.; Cao, Y.; Dong, L. Tide and Wave Measurement Based on High Precision Dynamic GNSS Technology. In Proceedings of the 40th Asian Conference on Remote Sensing, Daejeon, South Korea, 14–18 October 2019; pp. 14–18.
15. Gendron, B.C.; Chouaer, M.A.; Santerre, R.; Rondeau, M.; Seube, N. Wave measurements with a modified HydroBall® buoy using different GNSS processing strategies. *Geomatica* **2019**, *73*, 1–14.
16. Harigae, M.; Yamaguchi, I.; Kasai, T.; Igawa, H.; Nakanishi, H.; Murayama, T.; Iwanaka, Y.; Suko, H. Abreast of the waves: Open-sea sensor to measure height and direction. *GPS World* **2005**, *16*, 16-26.
17. Joodaki, G.; Nahavandchi, H.; Cheng, K. Ocean wave measurement using GPS buoys. *J. Geod. Sci.* **2013**, *3*, 163–172.
18. Waseda, T.; Sinchi, M.; Kiyomatsu, K.; Nishida, T.; Takahashi, S.; Asaumi, S.; Kawai, Y.; Tamura, H.; Miyazawa, Y. Deep water observations of extreme waves with moored and free GPS buoys. *Ocean Dyn.* **2014**, *64*, 1269–1280.
19. Krogstad, H.E.; Barstow, S.F.; Aasen, S.E.; Rodriguez, I. Some recent developments in wave buoy measurement technology. *Coast. Eng.* **1999**, *37*, 309–329.
20. Hou, D.; Hamada, M.; Yoo, Y.-J.; Kouguchi, N. Evaluation test result on wave direction measurement using GPS buoy. In Proceedings of the OCEANS 2006-Asia Pacific, Singapore, 16–19 May 2006; pp. 1–5.

21. Doong, D.-J.; Lee, B.-C.; Kao, C.C. Wave measurements using GPS velocity signals. *Sensors* **2011**, *11*, 1043–1058.
22. Thomson, J. Wave breaking dissipation observed with "SWIFT" drifters. *J. Atmos. Ocean. Technol.* **2012**, *29*, 1866–1882.
23. Terrill, E.; de Paolo, T. Development, testing and quality control of the Scripps Miniature Wave Buoy. In Proceedings of the Regional Marine Instrument Centre Coordination Meeting, Gulfport, MS, USA, 3 March 2016.
24. Qi, Z.; Li, S.; Li, M.; Dang, C.; Sun, D.; Zhang, D.; Liu, N.; Zhang, S. Research on the algorithm model for measuring ocean waves based on satellite gps signals in china. *Sensors* **2019**, *19*, 541.
25. Zhu, L.; Yang, L.; Xu, Y.; Yang, F.; Zhou, X. Retrieving wave parameters from GNSS buoy measurements using the PPP mode. *IEEE Geosci. Remote Sens. Lett.* **2020**, *19*, 1–5.
26. Yang, L.; Xu, Y.; Jiang, Y.; Mertikas, S.P.; Wang, Z.; Zhu, L.; Liu, N.; Lin, L. Retrieval of Ocean Wave Characteristics via Single-Frequency Time-Differenced Carrier Phases From GNSS Buoys. *IEEE Trans. Geosci. Remote Sens.* **2024**, *62*, 1–12.
27. Xue, C.; Guo, J.; Jiang, S.; Wang, Y.; Guo, Y.; Li, J. Performance Characteristics of Newly Developed Real-Time Wave Measurement Buoy Using the Variometric Approach. *J. Mar. Sci. Eng.* **2024**, *12*, 2032.
28. Gu, H.; Zhu, X.; Shan, R.; Zang, J.; Qian, L.; Lin, P. Evaluation of a GNSS for wave measurement and directional wave spectrum analysis. *Ocean Eng.* **2023**, *270*, 113683.
29. Peláez-Zapata, D.; Pakrashi, V.; Dias, F. Ocean wave directional distribution from GPS buoy observations off the west coast of Ireland: Assessment of a wavelet-based method. *J. Atmos. Ocean. Technol.* **2024**, *41*, 749–765.
30. Wang, J.; Chang, X.; Tu, R.; Yan, S.; Wang, S.; Zhang, P. Retrieval of Wave Parameters from GNSS Buoy Measurements Using Spectrum Analysis: A Case Study in the Huanghai Sea. *Remote Sens.* **2025**, *17*, 2869.
31. Raghukumar, K.; Chang, G.; Spada, F.; Jones, C.; Janssen, T.; Gans, A. Performance characteristics of "Spotter," a newly developed real-time wave measurement buoy. *J. Atmos. Ocean. Technol.* **2019**, *36*, 1127–1141.
32. Thomson, J.; Bush, P.; Castillo Contreras, V.; Clemett, N.; Davis, J.; de Klerk, A.; Iseley, E.; Rainville, E.J.; Salmi, B.; Talbert, J. Development and testing of microSWIFT expendable wave buoys. *Coast. Eng. J.* **2024**, *66*, 168–180.
33. Collins, C.O.; Dickhudt, P.; Thomson, J.; De Paolo, T.; Otero, M.; Merrifield, S.; Terrill, E.; Schonau, M.; Braasch, L.; Paluszkiewicz, T. Performance of moored GPS wave buoys. *Coast. Eng. J.* **2024**, *66*, 17–43.
34. Montenbruck, O.; Steigenberger, P.; Hauschild, A. Multi-GNSS signal-in-space range error assessment–Methodology and results. *Adv. Space Res.* **2018**, *61*, 3020–3038.
35. Valk, M.; Savenije, H.; Tiberius, C.; Luxemburg, W. Determining slack tide with a GPS receiver on an anchored buoy. *Hydrol. Earth Syst. Sci.* **2014**, *18*, 2599–2613.
36. Yan, X.; Liu, C.; Jiang, M.; Yang, M.; Feng, W.; Zhong, M.; Peng, L. Performance analysis of oceanographic research vessel precise point positioning based on BDS/GNSS RTK receivers. *Measurement* **2023**, *211*, 112637.
37. Di, M.; Guo, B.; Ren, J.; Wu, X.; Zhang, Z.; Liu, Y.; Liu, Q.; Zhang, A. GNSS Real–Time Precise Point Positioning in Arctic Northeast Passage. *J. Mar. Sci. Eng.* **2022**, *10*, 1345.
38. Geng, J.; Teferle, F.N.; Meng, X.; Dodson, A. Kinematic precise point positioning at remote marine platforms. *GPS Solut.* **2010**, *14*, 343–350.
39. Weng, D.; Ji, S.; Lu, Y.; Chen, W.; Li, Z. Improving DGNSS performance through the use of network RTK corrections. *Remote Sens.* **2021**, *13*, 1621.
40. Kim, J.; Song, J.; No, H.; Han, D.; Kim, D.; Park, B.; Kee, C. Accuracy improvement of DGPS for low-cost single-frequency receiver using modified Flächen Korrektur parameter correction. *ISPRS Int. J. Geo-Inf.* **2017**, *6*, 222.
41. Bisnath, S.; Wells, D.; Howden, S.; Dodd, D.; Wiesenburg, D.; Stone, G. Development of an operational RTK GPS-equipped buoy for tidal datum determination. *Int. Hydrogr. Rev.* **2004**, *5*, 54-64.
42. Lin, Y.-P.; Huang, C.-J.; Chen, S.-H.; Doong, D.-J.; Kao, C.C. Development of a GNSS buoy for monitoring water surface elevations in estuaries and coastal areas. *Sensors* **2017**, *17*, 172.
43. Sun, W.; Zhou, X.; Fu, Y.; Wang, Z.; Zhou, D. Monitoring Tides with GNSS Buoys in Open Sea Areas. In Proceedings of the International Workshop on Environment and Geoscience , Hangzhou, China, 15–17 June 2018.
44. Larsen, S.S.; Jensen, A.B.; Olesen, D.H. Characterization of carrier phase-based positioning in real-world jamming conditions. *Remote Sens.* **2021**, *13*, 2680.
45. Tamimi, R.; Toth, C. Assessing the viability of PPK techniques for accurate mapping with UAS. *Int. Arch. Photogramm. Remote Sens. Spat. Inf. Sci.* **2023**, *48*, 479–488.
46. Haddadi Amlashi, H.; Samadzadegan, F.; Dadrass Javan, F.; Savadkouhi, M. Comparing the accuracy of GNSS positioning variants for UAV based 3D map generation. *Int. Arch. Photogramm. Remote Sens. Spat. Inf. Sci.* **2020**, *43*, 443–449.

47. Harigae, M.; Yamaguchi, I.; Kasai, T.; Igawa, H.; Nakanishi, H.; Murayama, T.; Iwanaka, Y.; Suko, H. A low-cost GPS-based wave height and direction sensor for marine safety. In Proceedings of the 17th International Technical Meeting of the Satellite Division of The Institute of Navigation (ION GNSS 2004), Long Beach, CA, USA, 21–24 September 2004; pp. 1234–1245.
48. Angrisano, A.; Cappello, G.; Gaglione, S.; Gioia, C. Velocity Estimation Using Time-Differenced Carrier Phase and Doppler Shift with Different Grades of Devices: From Smartphones to Professional Receivers. *Algorithms* **2023**, *17*, 2.
49. Ji, L.; Sun, R.; Cheng, Q.; Wang, J. Evaluation of the performance of GNSS-based velocity estimation algorithms. *Satell. Navig.* **2022**, *3*, 18.
50. Freda, P.; Angrisano, A.; Gaglione, S.; Troisi, S. Time-differenced carrier phases technique for precise GNSS velocity estimation. *Gps Solut.* **2015**, *19*, 335–341.
51. Gioia, C.; Angrisano, A.; Gaglione, S. Galileo-based Doppler shifts and Time difference carrier phase: A static case demonstration. *Sensors* **2023**, *23*, 6828.
52. Ding, W.; Wang, J. Precise velocity estimation with a stand-alone GPS receiver. *J. Navig.* **2011**, *64*, 311–325.
53. Karimpour, A.; Chen, Q. Wind wave analysis in depth limited water using OCEANLYZ, A MATLAB toolbox. *Comput. Geosci.* **2017**, *106*, 181–189.
54. Panalaran, S.; Suntoyo. Study of Wave Parameters in the West side of Java Sea using Wave Spectral Analysis and Zero Up-Crossing Methods. In *Proceedings of the IOP Conference Series: Earth and Environmental Science*; IOP Publishing: Bristol, UK, 2023; p. 012034.
55. Vandever, J.P.; Siegel, E.M.; Brubaker, J.M.; Friedrichs, C.T. Influence of spectral width on wave height parameter estimates in coastal environments. *J. Waterw. Port Coast. Ocean Eng.* **2008**, *134*, 187–194.
56. Wyatt, L.R. The ocean wave directional spectrum. *Oceanography* **1997**, *10*, 85–89.
57. Grainger, J.P.; Sykulski, A.M.; Jonathan, P.; Ewans, K. Estimating the parameters of ocean wave spectra. *Ocean Eng.* **2021**, *229*, 108934.
58. Longuet-Higgins, M.S. The statistical analysis of a random, moving surface. *Philos. Trans. R. Soc. London Ser. A Math. Phys. Sci.* **1957**, *249*, 321–387.
59. Ardhuin, F.; Stopa, J.; Chapron, B.; Collard, F.; Husson, R.; Jensen, R.; Johannessen, J.; Mouche, A.; Passaro, M.; Quartly, G. Observing Sea States. *Front. Mar. Sci.* **2019**, *6*, 124.
60. Wyatt, L.R. Measuring the ocean wave directional spectrum 'First Five'with HF radar. *Ocean Dyn.* **2019**, *69*, 123–144.
61. Wang, D.W.; Hwang, P.A. Higher Fourier harmonics of the directional distribution of an equilibrium wave field under steady wind forcing. *J. Atmos. Ocean. Technol.* **2003**, *20*, 217–227.
62. Simanesew, A.W.; Krogstad, H.E.; Trulsen, K.; Nieto Borge, J.C. Bimodality of directional distributions in ocean wave spectra: A comparison of data-adaptive estimation techniques. *J. Atmos. Ocean. Technol.* **2018**, *35*, 365–384.
63. Das, S.; Subba Rao, S.; Yang, J. Spectral methods for small sample time series: A complete periodogram approach. *J. Time Ser. Anal.* **2021**, *42*, 597–621.
64. Blackman, R.B.; Tukey, J.W. The measurement of power spectra from the point of view of communications engineering—Part I. *Bell Syst. Tech. J.* **1958**, *37*, 185–282.
65. Bartlett, M.S. Periodogram analysis and continuous spectra. *Biometrika* **1950**, *37*, 1–16.
66. Welch, P. The use of fast Fourier transform for the estimation of power spectra: A method based on time averaging over short, modified periodograms. *IEEE Trans. Audio Electroacoust.* **1967**, *15*, 70–73.
67. Akaike, H. Power spectrum estimation through autoregressive model fitting. *Ann. Inst. Stat. Math.* **1969**, *21*, 407–419.
68. Liu, P.C. Wavelet spectrum analysis and ocean wind waves. In *Wavelet Analysis and Its Applications*; Elsevier: Amsterdam, The Netherlands, 1994; Volume 4, pp. 151–166.
69. Thomson, D.J. Spectrum estimation and harmonic analysis. *Proc. IEEE* **1982**, *70*, 1055–1096.
70. Huang, N.E.; Shen, Z.; Long, S.R.; Wu, M.C.; Shih, H.H.; Zheng, Q.; Yen, N.-C.; Tung, C.C.; Liu, H.H. The empirical mode decomposition and the Hilbert spectrum for nonlinear and non-stationary time series analysis. *Proc. R. Soc. London Ser. A Math. Phys. Eng. Sci.* **1998**, *454*, 903–995.
71. Earle, M. *Development of Algorithms for Separation of Sea and Swell*; MEC-87-1; National Data Buoy Center: Stennis Space Center, MS, USA, 1984.
72. Wang, D.W.; Hwang, P.A. An operational method for separating wind sea and swell from ocean wave spectra. *J. Atmos. Ocean. Technol.* **2001**, *18*, 2052–2062.
73. Gilhousen, D.B.; Hervey, R. Improved estimates of swell from moored buoys. In *Ocean Wave Measurement and Analysis (2001)*; ASCE: Reston, VA, USA, 2002; pp. 387–393.

74. Portilla, J.; Ocampo-Torres, F.J.; Monbaliu, J. Spectral partitioning and identification of wind sea and swell. *J. Atmos. Ocean. Technol.* **2009**, *26*, 107–122.
75. Hwang, P.A.; Ocampo-Torres, F.J.; García-Nava, H. Wind sea and swell separation of 1D wave spectrum by a spectrum integration method. *J. Atmos. Ocean. Technol.* **2012**, *29*, 116–128.
76. Meng, W.; Li, S.; Wang, X.; Jiang, H. Wind-sea and swell separation of 1D wave spectrum by deep learning. *Ocean Eng.* **2023**, *270*, 113672.
77. Gao, Y.; Schmitt, F.G., Hu, J., Huang, Y. Probability-based wind-wave relation. *Front. Mar. Sci* **2023**, *9*, 1085340.
78. Gerling, T.W. Partitioning sequences and arrays of directional ocean wave spectra into component wave systems. *J. Atmos. Ocean. Technol.* **1992**, *9*, 444–458.
79. Hasselmann, S.; Lionello, P.; Hasselmann, K. An optimal interpolation scheme for the assimilation of spectral wave data. *J. Geophys. Res. Oceans* **1997**, *102*, 15823–15836.
80. Voorrips, A.; Makin, V.; Hasselmann, S. Assimilation of wave spectra from pitch—and—roll buoys in a North Sea wave model. *J. Geophys. Res. Oceans* **1997**, *102*, 5829–5849.
81. Hanson, J.L.; Phillips, O.M. Automated analysis of ocean surface directional wave spectra. *J. Atmos. Ocean. Technol.* **2001**, *18*, 277–293.
82. Tracy, B.; Devaliere, E.-M.; Hanson, J.; Nicolini, T.; Tolman, H. Wind sea and swell delineation for numerical wave modeling. In Proceedings of the 10th international workshop on wave hindcasting and forecasting & coastal hazards symposium, Oahu, HI, USA, 11–16 November 2007; p. 1442.
83. Ailliot, P.; Maisondieu, C.; Monbet, V. Dynamical partitioning of directional ocean wave spectra. *Probabilistic Eng. Mech.* **2013**, *33*, 95–102.
84. Chen, Z.; Zhang, L.; Zhao, C.; Chen, X.; Zhong, J. A practical method of extracting wind sea and swell from directional wave spectrum. *J. Atmos. Ocean. Technol.* **2015**, *32*, 2147–2159.
85. Wyatt, L.R.; Green, J. Swell and wind-sea partitioning of HF radar directional spectra. *J. Oper. Oceanogr.* **2024**, *17*, 28–39.
86. Zheng, Z.; Dong, G.; Dong, H.; Ma, X.; Tang, M. Research on the methods for separating wind sea and swell from directional wave spectra in finite-depth waters. *Ocean Dyn.* **2024**, *74*, 113–131.
87. Lee, Y.-C.; Doong, D.-J. Duration-limited growth method for wind sea and swell separation of directional wave spectrum. *Ocean Eng.* **2025**, *329*, 121182.
88. Patra, S.K.; Jena, B. Inter-comparison of wave measurement by accelerometer and GPS wave buoy in shallow water off Cuddalore, east coast of India. *Indian J. Geo-Mar. Sci.* **2014**, *43*, 45–49.
89. Beckman, J.N.; Long, J.W. Quantifying errors in wind and wave measurements from a compact, low-cost wave buoy. *Front. Mar. Sci.* **2022**, *9*, 966855.
90. Hansen, J.E.; Cuttler, M.V.; Lowe, R.J.; Young, I.; Ierodiaconou, D.; Hatcher, M.; Boldaji, S. Spectral and time-domain comparison of GNSS and accelerometer wave buoys. *Coast. Eng.* **2026**, *211*, 105049.
91. Yurovsky, Y.Y.; Kudinov, O.B. Methods and errors of wave measurements using conventional inertial motion units. *Phys. Oceanogr.* **2025**, *32*, 63–83.
92. Bender III, L.C.; Guinasso Jr, N.; Walpert, J.N.; Howden, S.D. A comparison of methods for determining significant wave heights—Applied to a 3-m discus buoy during Hurricane Katrina. *J. Atmos. Ocean. Technol.* **2010**, *27*, 1012–1028.
93. Huh, Y.; Hwang, C.-S.; Kim, D.H.; Heo, S.; Kim, J.-Y.; Lee, K.-W.; Hong, S.-D. Performance evaluation of wave observation system using GPS. *J. Korean Soc. Mar. Environ. Energy* **2012**, *15*, 357–362.
94. Watson, C.; Coleman, R.; White, N.; Church, J.; Govind, R. Absolute calibration of TOPEX/Poseidon and Jason-1 using GPS buoys in bass strait, Australia special issue: Jason-1 calibration/validation. *Mar. Geod.* **2003**, *26*, 285–304.
95. Watson, C.; White, N.; Church, J.; Burgette, R.; Tregoning, P.; Coleman, R. Absolute calibration in bass strait, Australia: TOPEX, Jason-1 and OSTM/Jason-2. *Mar. Geod.* **2011**, *34*, 242–260.
96. Zhou, B.; Watson, C.; Beardsley, J.; Legresy, B.; King, M.A. Development of a GNSS/INS buoy array in preparation for SWOT validation in Bass Strait. *Front. Mar. Sci.* **2023**, *9*, 1093391.
97. Ho, A.; Wang, J.; Haines, B.; Wu, A.; Stalin, S. In situ validation of small--scale spatial variability in significant wave height observations from SWOT. *Earth Space Sci.* **2025**, *12*, e2025EA004286.
98. Hay, A.; Watson, C.; Legresy, B.; King, M.; Zhou, B.; Beardsley, J.; Bohé, A. In situ geometric validation of SWOT satellite observations in Bass Strait, Australia. *Earth Space Sci.* **2025**, *12*, e2025EA004326.
99. Perry, B.; Huisman, B.; Antolínez, J.A.; Hesp, P.A.; Miot da Silva, G. Impacts of large scale climate modes on the current and future bimodal wave climate of a semi-protected shallow gulf. *Front. Mar. Sci.* **2024**, *11*, 1364736.

100. Thomas, J.; George, J.; Van Proosdij, D.; Murphy, E. Wave dynamics and potential longshore sediment transport at Shippagan, Gulf of St Lawrence: Insight into seasonal variability and extreme weather events. *Front. Mar. Sci.* **2025**, *12*, 1579807.
101. Di, M.; Guo, B.; Li, M.; Liu, H.; Li, X.; Ma, D.; Zhang, A. Low-Cost Multi-Antenna GNSS Buoys for Marine Environment Sensing. In *Proceedings of the Journal of Physics: Conference Series*; IOP Publishing: Bristol, UK, 2026; p. 012085.
102. Hole, L.R.; Fer, I.; Peddie, D. Directional wave measurements using an autonomous vessel. *Ocean Dyn.* **2016**, *66*, 1087–1098.
103. Jensen, R.E.; Swail, V.; Bouchard, R.H. Quantifying wave measurement differences in historical and present wave buoy systems. *Ocean Dyn.* **2021**, *71*, 731–755.
104. Saetre, C.; Tholo, H.; Hovdenes, J.; Kocbach, J.; Hageberg, A.A.; Klepsvik, I.; Aarnes, O.J.; Furevik, B.R.; Magnusson, A.K. Directional wave measurements from navigational buoys. *Ocean Eng.* **2023**, *268*, 113161.
105. Thomson, J.; Talbert, J.; De Klerk, A.; Brown, A.; Schwendeman, M.; Goldsmith, J.; Thomas, J.; Olfe, C.; Cameron, G.; Meinig, C. Biofouling effects on the response of a wave measurement buoy in deep water. *J. Atmos. Ocean. Technol.* **2015**, *32*, 1281–1286.
106. Hope, G.; Seldal, T.I.; Rabault, J.; Bryhni, H.T.; Bohlinger, P.; Björkqvist, J.-V.; Nordam, T.; Kleven, A.; Mostaani, A.; Furevik, B.R. SFY—A lightweight, high-frequency, and phase-resolving wave buoy for coastal waters. *J. Atmos. Ocean. Technol.* **2025**, *42*, 133–154.
107. Benetazzo, A.; Bergamasco, F.; Barbariol, F.; Ferla, M.; Nardone, G.; Orasi, A.; Picone, M.; Stevanin, A.; Marchitiello, A.; Pavan, T. Evaluation of the 3D response and performance of an operational wave buoy for coastal wave monitoring. *Coast. Eng.* **2025**, *200*, 104756.
108. Thomson, J.; Girton, J.B.; Jha, R.; Trapani, A. Measurements of directional wave spectra and wind stress from a wave glider autonomous surface vehicle. *J. Atmos. Ocean. Technol.* **2018**, *35*, 347–363.

Disclaimer/Publisher's Note: The statements, opinions and data contained in all publications are solely those of the individual author(s) and contributor(s) and not of MDPI and/or the editor(s). MDPI and/or the editor(s) disclaim responsibility for any injury to people or property resulting from any ideas, methods, instructions or products referred to in the content.